IOP Publishing and International Atomic Energy Agency Nuclear Fusion
Nucl. Fusion **51** (2011) 033004 (20pp) doi:10.1088/0029-5515/51/3/033004

Calculation of the non-inductive current profile in high-performance NSTX plasmas

S.P. Gerhardt[1], E. Fredrickson[1], D. Gates[1], S. Kaye[1], J. Menard[1], M.G. Bell[1], R.E. Bell[1], B.P. Le Blanc[1], H. Kugel[1], S.A. Sabbagh[2] and H. Yuh[3]

[1] Princeton Plasma Physics Laboratory, Princeton, NJ 08543, USA
[2] Columbia University, New York, NY 10027, USA
[3] Nova Photonics, Princeton, NJ 08540, USA

Received 7 September 2010, accepted for publication 20 January 2011
Published 18 February 2011
Online at stacks.iop.org/NF/51/033004

Abstract
The constituents of the current profile have been computed for a wide range of high-performance plasmas in NSTX (Ono *et al* 2000 *Nucl. Fusion* **40** 557); these include cases designed to maximize the non-inductive fraction, pulse length, toroidal-β or stored energy. In the absence of low-frequency MHD activity, good agreement is found between the reconstructed current profile and that predicted by summing the independently calculated inductive, pressure-driven and neutral beam currents, without the need to invoke any anomalous beam ion diffusion. Exceptions occur, for instance, when there are toroidal Alfvén eigenmode avalanches or coupled $m/n = 1/1 + 2/1$ kink-tearing modes. In these cases, the addition of a spatially and temporally dependent fast-ion diffusivity can reduce the core beam current drive, restoring agreement between the reconstructed profile and the summed constituents, as well as bringing better agreement between the simulated and measured neutron emission rate. An upper bound on the fast-ion diffusivity of $\sim$0.5–1 m^2 s^{-1} is found in 'MHD-free' discharges, based on the neutron emission, the time rate of change in the neutron signal when a neutral beam is stepped and reconstructed on-axis current density.

(Some figures in this article are in colour only in the electronic version)

1. Introduction

The spherical torus [1] has been proposed as the fusion core for devices designed to test high heat flux plasma material interactions [2], study fusion nuclear science (FNS) [3–7] or generate electricity [8, 9]. The interest in this configuration was spawned from theoretical work like that discussed in [1]. The first larger experimental test of the ST was the START [10] device, which achieved values of toroidal β exceeding 30% [11, 12] under neutral beam (NB) heating [13]. These results lead to further theoretical studies of the achievable equilibria for the ST [14, 15], producing configurations with virtually 100% of the toroidal current provided by the pressure-driven bootstrap current [16–20]; these configurations were stable to both high-n ballooning and $n = 1$–3 kink modes (with a nearby conducting wall). The START results, along with these theory developments, motivated the construction of the $I_P = 1$ MA class STs NSTX (National Spherical Torus Experiment) [21] and MAST (Mega-Ampere Spherical Torus) [22]. Results from these two devices have then paved the way for the design of the next-step devices noted above.

Part of the design process for these next-step spherical torii is to define the shape and magnitude of the toroidal current density profile, and specify the current drive tools that will provide that current. The designers assume that the current profile can be predicted as the sum of pressure-driven currents, neutral beam driven currents, currents driven by radiofrequency and microwave means, and potentially some residual inductive current. It is the purpose of this paper to study the make-up of these different toroidal current sources in a wide variety of high-performance plasmas in the NSTX.

Calculation of the individual components of the current profile is a well-established process in conventional aspect ratio tokamaks. The inductive current is calculated from the loop voltage profile [23] and neoclassical resistivity [24]. The bootstrap current can be calculated from simple analytic models such as those in [24, 25] or multi-species models as in the NCLASS code [26]. The neutral beam current [27–33] is often calculated from Monte Carlo codes, with NUBEAM [34, 35] a commonly used example. Code packages also exist to calculate the current driven by RF and microwave current drive tools. Calculations of this sort have been applied to

most large tokamaks, with an incomplete list including DIII-D [23, 36–51], JET [52–56], JT-60 [57, 58], TFTR [59] and ASDEX-Upgrade [60]. These calculations have often assumed classical physics for the beam ions, though there are cases where this assumption may not be warranted. For instance, tearing modes have been shown to modify the neutral beam current profile [37, 42], consistent with observations of fast-ion loss due to these instabilities [61, 62]. Alfvén modes have also been shown to modify the current profile [63, 64]. Recently, evidence from DIII-D [49, 50] and ASDEX-Upgrade [60] has indicated that the electrostatic turbulence responsible for thermal plasma transport may also lead to radial diffusion of the injected fast ions.

Calculations of this sort are less well established in the spherical torus configuration. Experiments in MAST [65] used upward and downward shifted L-mode plasmas in order to study off-axis neutral beam current drive. The off-axis NBCD helped avoid harmful MHD instabilities, and extended the operational window for the device. At lower injected powers ($P_{\rm inj} < 2$ MW), TRANSP [66] simulations of the neutron rate and stored energy agreed well with measurement. When the neutral beam power was increased, fishbone modes were observed, and an *ad hoc* fast-ion diffusivity was required in TRANSP to match the measured neutron emission rate and stored energy.

A first assessment of the current profile constituents in high-β NSTX H-mode plasmas was published in [67, 68]. Reference [67] examined a single discharge in detail. It showed that in the absence of low-frequency MHD, the reconstructed current profile could indeed be understood as the sum of neoclassical pressure-driven currents, inductive currents and beam driven currents, with purely (neo)classical physics for all calculations. During the later phase of the discharge, an $m/n = 1/1$ rotating core MHD mode grew and saturated; anomalous fast-ion diffusion was required to understand the current profile reconstruction during this phase. A similar calculation was reported in [69], where good agreement was found between the current profile reconstructed from Grad–Shafranov solutions and that summed from calculations of the current profile constituents; only a small discrepancy in the on-axis current density was reported. Calculations of the non-inductive fraction in NSTX using TRANSP and NUBEAM have also been reported in [70–73]. These studies used kinetic profiles as inputs to the code, and showed good matches between the measured and simulated neutron emission, but did not have the detailed analysis and crosschecking of the current profile described here.

This paper focuses on two important questions, expanding on the previous MAST and NSTX papers in a number of important ways. First, under what conditions can the NSTX current profile be understood as the sum of neoclassical current drive sources? Second, what is the effect of some typical MHD events on the fast-ion driven current, and what is the upper bound on the fast-ion diffusivity in discharges that do not have low-frequency MHD?

The current profile composition is studied for a range of high-performance discharges over a wide range of q_{95} (q_{95} is the safety factor at the magnetic surface that encloses 95% of the enclosed poloidal flux); these include high-q_{95}, high-$\beta_{\rm P}$ discharges optimized for highest non-inductive fraction, medium-q_{95} cases optimized for long pulse and low-q_{95} cases optimized for high toroidal β and/or maximal stored energy. In the high-q_{95}, high-$\beta_{\rm P}$ case, we evaluate discharges that are free of MHD, that have TAE avalanches and that have coupled $m/n = 2/1 + 1/1$ modes; the effects of these modes on the current profile are addressed. The upper bound for anomalous fast-ion diffusivity in plasmas without low-frequency MHD is discussed. Overall, the results of this paper are cautiously optimistic with respect to current profile prediction using neoclassical physics only; however, a number of issues that may complicate this conclusion are discussed.

The rest of this paper is organized as follows. Section 2 describes the NSTX device and analysis techniques that are used. Section 3 examines the evolution of the neutron emission rate when the neutral beams are stepped on and off, by comparing the measured evolution with that predicted by the NUBEAM module within TRANSP. Section 4 studies the reconstruction of the current profile from constituent parts, for a series of high-q_{95}, high-$\beta_{\rm P}$ discharges designed to maximize the non-inductive fraction. The effects of TAE avalanches and rotating $n = 1$ kink/tearing modes on the current profile are illustrated. Section 5 describes similar analysis of a discharge optimized for maximum pulse length. Section 6 describes current profile analysis for discharges designed to maximize the toroidal β and stored energy. Section 7 contains a discussion of an upper bound on the fast-ion diffusivity in MHD-free discharges. Section 8 contains a discussion and summary of these results.

2. The NSTX device and analysis techniques

NSTX [21] is a medium size spherical torus designed to test the benefits of extending the traditional tokamak to low aspect ratio [1]. The geometric major radius of a typical high-β plasma is $R_0 \approx 0.85$ m, with a Shafranov-shifted magnetic axis radius of 1.05–1.1 m. The minor radius is typically 60 cm, yielding typical aspect ratios R_0/a of 1.3–1.5. The plasma currents from discharges in this paper span the typical NSTX operating space of $0.7 < I_{\rm P}({\rm MA}) < 1.3$; toroidal field strengths up to 0.55 T are available, though this paper addresses discharges with $0.4 < |B_{\rm T}|({\rm T}) < 0.48$. The plasmas in this paper are heated with up to 6 MW of co-injected neutral beam power, and all have $\beta_{\rm N}$ values at or above the $n = 1$ no-wall limit. The neutral beam (NB) injection system is composed of a single beamline with three independent NB sources. These sources are referred to as sources A, B and C, with tangency radii of approximately 70, 60 and 50 cm, respectively. Further information regarding the neutral beam geometry can be found in [74].

The discharges in this paper were generally optimized to push a high-performance boundary, such as highest non-inductive fraction, longest possible pulse or highest stored energy. These goals are generally facilitated by running with high elongation (κ) and high triangularity (δ) [75, 76]. This is illustrated in the plasma cross-section for high-$\beta_{\rm P}$ discharge 133964 in figure 1. Note that the shape control in NSTX is provided by a combination of realtime equilibrium reconstruction and plasma boundary control with an 'ISOFLUX' algorithm [77]. Also, dynamic error field correction (DEFC) of $n = 1$ error fields [78], static correction

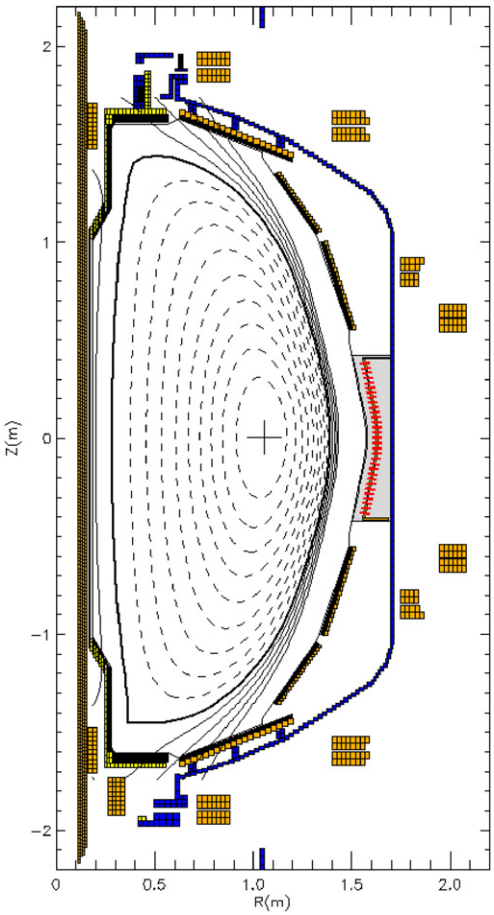

Figure 1. Plasma cross-section for the discharge with the lowest flat-top average loop voltage of any H-mode NB heated discharge in NSTX (133964). This discharge will be studied in detail in sections 4, 7 and 8. The shape is typical of the discharges described in this paper.

of $n = 3$ error fields [79] and fast RWM control [80, 81] are important for improving the overall stability and reliability of these discharge scenarios. The stability and transport properties of these discharges, and comparison with previously developed high-performance NSTX plasmas, are discussed in [82].

Lithium conditioning of the graphite plasma facing components is used for all plasmas described in this paper. Two lithium evaporators deposit lithium vapour on the vessel floor; this lithium primarily coats the divertor, and to a lesser extent, the centre column and lower passive plates [83, 84]. This conditioning has many beneficial effects, including the elimination of ELMs [85], reduction in electron transport [86] and the lowering of the H-mode threshold [87]. The elimination of ELMs, however, typically leads to an uncontrolled accumulation of impurities [84], including metals and carbon from the plasma facing components. Note that these lithium induced changes can affect the non-inductive current drive in a number of ways. For comparable density, the higher T_e increases the fast-ion slowing down time (and thus the beam current drive), while also increasing the pressure and bootstrap fraction, since $f_{BS} \propto \beta_P$. The higher Z_{eff} increases the beam current drive (see equation (2) below), though at the expense of lower β compared with a plasma with similar electron content and lower Z_{eff}. The detailed study of these lithium effects is, however, outside the scope of this paper.

The comprehensive NSTX diagnostic set is of critical importance in deriving the results in this paper. The electron temperature and density are measured by a 30 point Thomson scattering system [88] with measurement points along the midplane on both sides of the magnetic axis. The ion temperature, carbon concentration and carbon toroidal velocity are measured by a 51 channel charge exchange recombination spectroscopy (CHERS) diagnostic measuring primarily on the outboard midplane; the deuterium profile is then inferred from the electron and carbon density profiles using quasi-neutrality and the assumption that no additional impurities are present. The magnetic field pitch angle is measured by a 16 channel motional Stark effect (MSE) diagnostic [89].

As implied above, the primary analysis method in this paper is composed of three steps. The first step is to 'reconstruct' the plasma current profile from Grad–Shafranov solutions that are constrained to match the available data. The second step is to compute the profiles of the inductive, neutral beam and pressure-driven currents from the reconstructions and measured plasma profiles. This third step is to sum these current profile constituents, and compare the sum with the reconstructed current density.

The Grad–Shafranov solutions in this paper are calculated with the code LRDFIT [90]. All such reconstructions shown in this paper are constrained by the external magnetics, diamagnetic flux measurement, E_R corrected MSE measurements and a T_e isotherm requirement (that is, solutions found by the code are constrained to have the same temperature on both the inside and outside of the magnetic surface at the midplane). The code is run to two different ways. The first method uses a version of the Grad–Shafranov equation with rotational corrections to the equilibrium, and is indicated in this paper by the text 'LRDFIT09' in the figures. In other cases, we have solved the traditional Grad–Shafranov equation without rotation, but with an additional constraint on the pressure profile; these are indicated by the text 'LRDFIT12'. In these cases, the measured total kinetic pressure, from Thomson scattering and CHERS, is used to constraint the MHD pressure profile in the outer 1/3 of the plasma, where the fast-ion pressure should be small; this provides a very strong constraint on the pedestal height and edge current density. The pressure profile over the inner 2/3 of the plasma is not constrained, since we do not know, within the confines of this code, the fast-ion pressure profile. We have generally favoured the '09' runs, as they converge more easily. However, we have found that the '12' runs are sometimes required in order to reconstruct details in the profile shapes.

The time-series of reconstructions so computed is then used to calculate the toroidal electric field $E_\phi = (\mathrm{d}\psi/\mathrm{d}t)/R$ and loop voltage $V_{loop} = ((2\pi\langle E_\varphi B_\varphi\rangle)/(F\langle R^{-2}\rangle))$. The parallel inductive current density is then computed as $\langle J_\parallel B\rangle_{ind}/\langle B\cdot\nabla\phi\rangle = \sigma_{neoc}(V_{loop}/2\pi)$, where σ_{neoc} is computed from the Sauter formulation [24]. Here, ψ is the poloidal flux.

The relevant pressure-driven currents include the toroidal components of the Pfirsch–Schlueter and diamagnetic currents [19] and the bootstrap currents [16–20, 25]. The latter is a neoclassical current that has the potential to provide most or

all of the current required to sustain the tokamak equilibrium. Simplistically, it can be understood as the parallel current that must flow to cancel the poloidal part of the perpendicular (diamagnetic) current, since poloidal currents are strongly damped by viscosity due to the field variation in that direction [20]. The beneficial effect of stronger toroidal field (TF) can be understood in this picture by observing that as the TF is increased, a larger part of the perpendicular currents will be in the poloidal direction, and larger parallel current must flow in order to have a substantial poloidal component. The particular formulation of the bootstrap current used in this paper is presented in [24, 91], and can be expressed as

$$\langle J_\parallel B\rangle = F(\psi)p_e(L_{31}A_1 + L_{32}A_2 + L_{34}A_4), \qquad (1)$$

where the A_i are functions of the kinetic profile gradients as

$$A_1 = \frac{1}{p_e}\frac{\partial p_e}{\partial \psi} + \frac{1}{p_e}\frac{\partial p_i}{\partial \psi},$$

$$A_2 = \frac{1}{T_e}\frac{\partial T_e}{\partial \psi}, \qquad A_2^i = \frac{1}{T_i}\frac{\partial T_i}{\partial \psi},$$

$$A_4 = \alpha\frac{1 - R_{p_e}}{R_{p_e}}A_2^i.$$

The L_{ij} are functions of the charge number, normalized collisionality and trapped particle fraction, and are defined in [24]. The expression in [1] is evaluated using either TRANSP or with standalone routines.

The final significant term in the NSTX current drive mix is that due to neutral beam current drive [27–33, 92, 93]. This current is due to toroidally circulating fast ions, and can be calculated as

$$\langle j_{NB}\cdot B\rangle = \langle j_{f\parallel}\cdot B\rangle\left[1 - \frac{Z_B}{Z_{eff}}(1 - G(Z_{eff},\varepsilon))\right]. \qquad (2)$$

Here, $j_{f\parallel}$ is the fast-ion current, Z_B is the charge of the injected beam ion charge and G is a function of Z_{eff} and aspect ratio, whose most complete definition can be found in [33]. The term $(Z_B/Z_{eff})(1 - G(Z_{eff},\varepsilon))$ accounts for electrons flowing in the opposite direction and partially cancelling the fast-ion current [9, 33]. We have used the NUBEAM [34, 35] code within TRANSP to compute the neutral beam current drive for all cases in this paper. This code has the ability to impose both an additional 'anomalous' radial diffusion and radial convection on the fast-ion population, as a function of both space and time. This provision has been used to simulate the effects of various MHD modes on the fast-ion population.

A few other details are worth mentioning. The error bars in most figures are calculated from the standard deviation of a given signal or calculation within the specified averaging window. Thus, they do not incorporate the effects of any systematic errors. Some sources of systematic error, including profile parametrization and centrifugal effects, are discussed in section 7. All profiles are plotted against the variable ρ_{pol}, a minor radius variable defined as $\rho_{pol} = \sqrt{(\psi - \psi_{core})/(\psi_{edge} - \psi_{core})}$.

3. Comparison of the measured and simulated neutron dynamics during beam steps

As noted above, the results in this paper rely heavily on TRANSP calculations of the neutral beam current. Before examining those calculations directly, it is useful to compare measurements and modelling of the neutron evolution before and after a step change in the neutral beam power. Previous experiments have studied the behaviour of 'dilute' populations of fast ions [32, 49, 50, 74], including studies in NSTX L-mode plasmas [74]. The latter study showed that the prompt loss and slowing down of fast ions in those plasmas were consistent with classical behaviour. This topic is revisited here in order to provide a (somewhat limited) validation of the neutral beam model in TRANSP for high-performance H-mode plasmas.

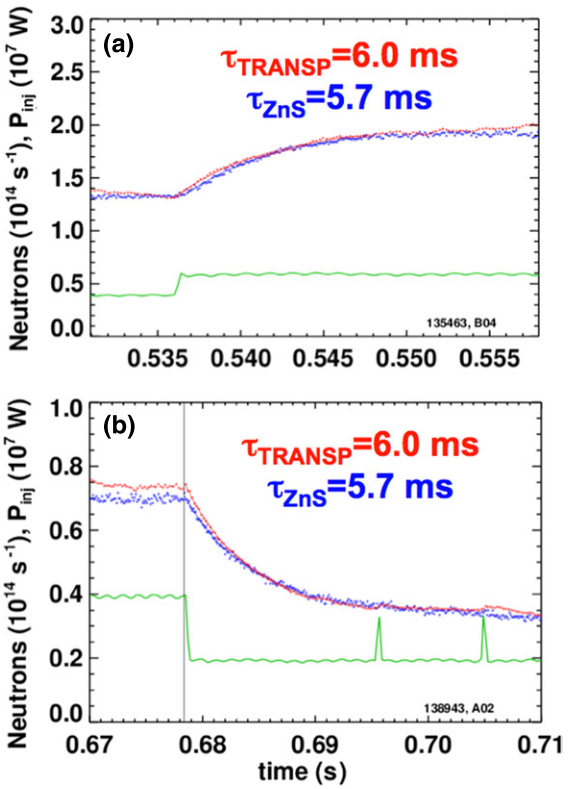

Figure 2. Example fits to the neutron emission (*a*) after a beam turn-on and (*b*) after a beam turn-off. The measured neutron emission is in blue, while the simulated emission is in red and the neutral beam power is in green. The fits are shown as solid lines through the data points.

The method here is that described in [74]. The neutron emission in NSTX is dominated by beam-target reactions. The increase in the neutron emission rate R_N (in N s^{-1}) when a beam is turned on is fit to $dR_N/dt = c - (R_N/\tau_R)$. The initial rise in the neutron signal is indicative of the prompt loss rate [74]. The decay of the neutron emission when a beam is turned off is fit to $dR_N/dt = -(R_N/\tau_D)$, and is indicative of the thermalization and slowing down of the fast ions. In each case, both the measurement and TRANSP simulation of the neutron emission are fit in an identical manner, such that the time-scales τ_D and τ_R can be compared between simulation and experiment. All fits in this section are from MHD-free phases of the discharge, and there is no anomalous fast-ion diffusivity in any calculation.

Example fits are shown in figure 2, for the beam turn-on in frame (*a*), and the beam turn-off in frame (*b*). The TRANSP simulations and measurements are in excellent agreement, for

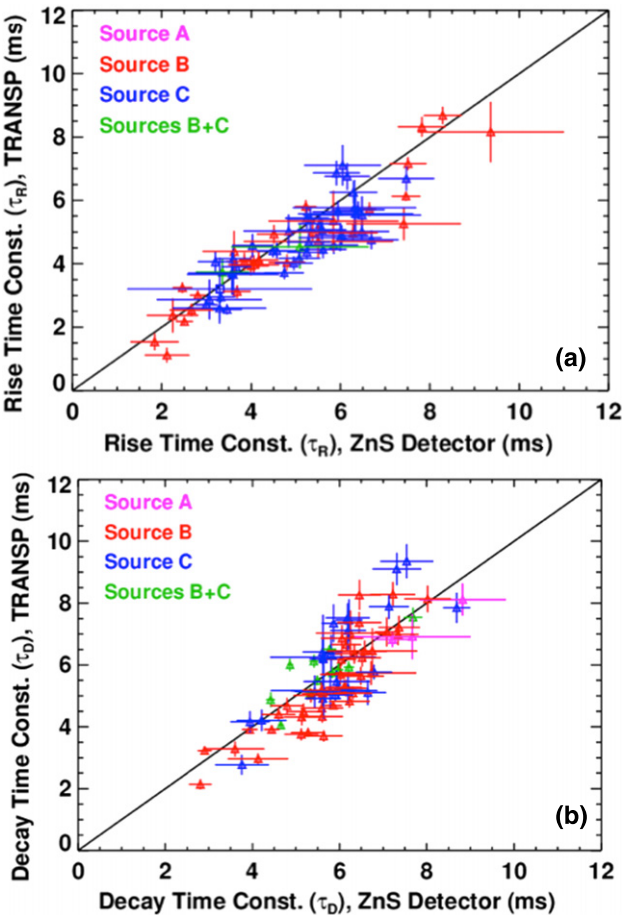

Figure 3. Comparison of the fit time constants for measurements and TRANSP simulations. Frame (*a*) shows the time constant associated with the beam turn-on (τ_R), while frame (*b*) shows the time constant associated with the turn-off (τ_D).

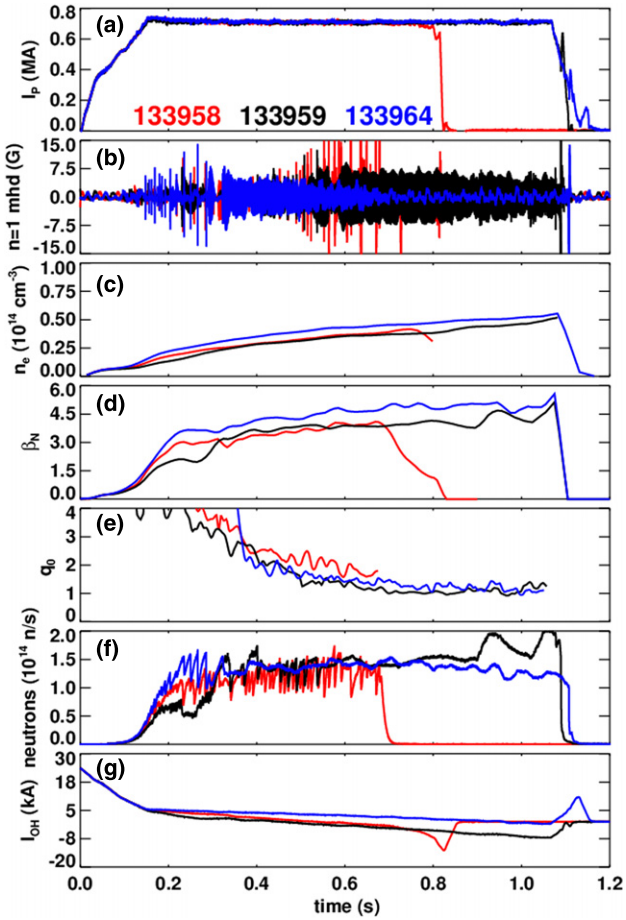

Figure 4. Time traces of three nearly adjacent discharges, showing the different MHD activity and resulting effects. Shown are (*a*) the plasma current, (*b*) the Mirnov-signal processed to detect odd-n MHD, (*c*) the line-average density, (*d*) β_N, (*e*) the reconstructed value of q_0, (*f*) the neutron emission and (*g*) the solenoid flux consumption. All three cases are heated with 6 MW of neutral beams; the beam sources are on until the end of discharges 133959 and 133964, but turn-off at $t = 0.67$ in discharge 133958.

both the absolute magnitude of the emission and the time-scale of the change, and the model equations fit the measurement and simulations quite well.

This process has been repeated for a large number of discharges where neutral beam modulations were used. Some of these were dedicated transport experiments, while others were discharges associated with the development of β_N control via neutral beam modulation. The results of these fits are shown in figure 3, with fits to the rise time constant in frame (*a*) and to the decay time constant in frame (*b*). Good agreement between measured and simulated values is found in both cases.

The results presented here provide some validation of the NUBEAM model with TRANSP to predict the neutral beam current drive in MHD-free H-mode discharges. In particular, the neutron emission is most sensitive to the highest energy beam ions, which are also most effective at carrying the current. Also, this comparison of measured and simulated time-scales is valid independent of any calibration factors associated with the neutron detector hardware. Note, however, that the present fast-ion D_α (FIDA) diagnostic [94], and the toroidally viewing upgrade to the system presently being designed [95], will allow much more detailed validation of the TRANSP H-mode NBCD and fast-ion distribution function calculations.

4. Current profile reconstructions in high-q_{95}, high-β_P plasmas optimized for the highest non-inductive fraction

The first set of plasmas selected for study was optimized to have the highest possible non-inductive fraction, consistent with a reasonably long pulse. Since the bootstrap current increases with increasing toroidal field (see discussion in section 2), these discharges were run at a somewhat elevated toroidal field $B_T = 0.48$ T. The TF coil heating limit at this field limits the achievable flat-top duration to ~1 s. Note that these discharges were designed to study in greater detail the high-κ scenario first described in [73].

The performance of three nearby discharges in this sequence is shown in figure 4. The plasma current is 0.7 MA for all cases, as shown in frame (*a*) and all have q_{95} of ~14; the neutral beam heating power of 6 MW (not shown) is the same in all cases as well. The MHD activity is illustrated in frame (*b*), where the poloidal magnetic field detected at the vessel wall is processed to discriminate for odd-*n* signals (and is typically dominated by $n = 1$ fluctuations). The three discharges have

vastly different MHD activities, with 133958 experiencing a series of bursting MHD modes, 133959 succumbing to a large saturated $n = 1$ mode and 133964 exhibiting a long MHD-free period at the end of the pulse. Discharge 133964 has slightly larger fuelling and an earlier H-mode transition, both of which lead to it having higher density than the other cases.

The discharge without low-frequency MHD (133964) also has a higher value of β_N, defined as $\beta_N = \beta_T/(I_P/aB_T)$; this is indicative of the deleterious effects of the MHD modes on the global confinement in the other cases. Interestingly, this case has a lower value of the central temperature ($T_{e,0} = \sim$800 eV) compared with the other cases ($T_{e,0} = \sim$1100–1200 eV). The temperature profile is, however, broader; when coupled to the higher density, this case has a thermal stored energy that is ∼20% higher. The TRANSP simulations described below indicate that the fast-ion stored energy is 10–20% higher in 133964, despite the lower T_e and higher n_e, due to the effect of the MHD modes.

The evolution of the central safety factor is shown in frame (*e*), and two trends are immediately apparent: (i) the two discharges which last to ∼1 s duration have achieved a nearly fully evolved current profile and (ii) the red case with bursting MHD modes has a substantially higher central safety factor. The measured neutron emission from the plasma is illustrated in frame (*f*), and shows, for the red discharge, the abrupt loss of fast ions associated with the bursting MHD modes. Finally, the solenoid current is shown in frame (*g*), as an indication of the non-inductive current behaviour in these cases. Compared with the black and red cases, the blue discharge (133964) uses solenoid flux at a much reduced rate, indicating that the non-inductive fraction will be larger for this discharge. The major goal of the analysis in this section is to understand how the MHD illustrated in frame (*b*) impacted the flux consumption indicated in frame (*g*). These three discharges will thus be studied in the following three sub-sections.

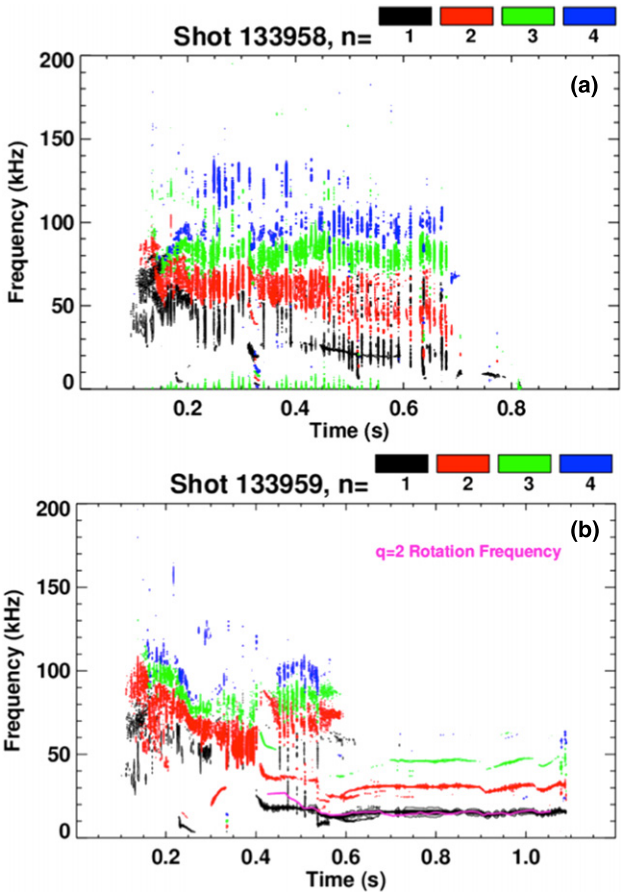

Figure 5. Spectrograms for the two cases in figure 4 with strong MHD. Shown are (*a*) 133958, with strong TAE avalanches and (*b*) 133959, with a saturated core $n = 1$ mode. Also shown in (*b*) is the rotation frequency of the $q = 2$ surface.

4.1. Bursting MHD modes

We consider first the discharge with bursting MHD modes (133958). A spectrogram of the MHD activity for this discharge is shown in figure 5(*a*). There are clear overlapping bursting modes, often with simultaneous toroidal mode numbers 1 through 4. These modes have been previously identified as TAE avalanches [96, 97]. There is copious evidence for the transport of fast ions due to these instabilities [97], including the sharp drops in the neutron rate noted above and from the FIDA system [94]. Simulations of these avalanches in L-mode discharges using the NOVA-K [98, 99] and ORBIT [100] codes have been successful in matching the observed neutron rate drop [96].

In order to understand the effects of these modes on the current profile, we have chosen to simulate them using a temporally and spatially varying fast-ion diffusivity (D_{FI}). This approach was taken for a number of reasons. For instance, the reflectometer data used to select from among the NOVA-K eigenmodes [96] are not available in the H-mode discharges discussed here. Furthermore, even if we were to select a subset of these linear eigenfunctions, we would not have the appropriate information to scale them in order to compute the expected fast-ion transport and loss. Note, however, that a beam emission spectroscopy (BES) diagnostic was recently installed on NSTX [101], which should facilitate the detailed study of these instabilities in H-mode plasmas.

In order to simulate the effect of these modes on the current profile, the anomalous fast-ion diffusivity radial and temporal variation was specified to TRANSP as

$$D_{FI}(\rho_{pol}, t) = \frac{A_{FI}(t)}{2}\left[1 - \tanh\left(\frac{\rho_{pol} - w}{0.05}\right)\right] + D_{FI,DC}. \quad (3)$$

This form causes the D_{FI} to be higher in the plasma core than the edge, with the width of the large-D_{FI} region determined by the parameter w. The denominator in the tanh function was always set to 0.05 to provide a smooth but reasonably sharp roll-off of D_{FI} on either side of $\rho_{pol} = w$. The temporal variation of $A_{FI}(t)$ was set by associating the start time and duration of the measured modes to the start time and duration of periods with large A_{FI}. For this experimentally determined timing, scans of the radial width (w) and peak amplitude of the fast-ion diffusivity 'bursts' were performed. The 'optimal' combination of radial width and amplitude would match the average level of the neutron emission, the amplitude of the loss at each mode and the recovery rate of the neutron emission rate between the modes. Note that for a given TRANSP run, the width and amplitude of these impulsive diffusion phases were

identical, and only the timing set to match the data. Also, no effort was made to match the neutron rate drop for each mode (i.e. the parameters such as $A_{\rm FI}$ and w were not tailored for each individual burst). The fast-ion diffusivity was either set to zero or a small number for periods between the large 'bursts'. An example $D_{\rm FI}$ profile in radius and time is shown in figure 6(a). The radial width of the $D_{\rm FI}$ in this case is $w = 0.7$, with peak values of 50 $\rm m^2\,s^{-1}$ and a steady value between pulses ($D_{\rm FI,DC}$) of 1 $\rm m^2\,s^{-1}$.

Given these values for the fast-ion diffusivity, the results of the TRANSP calculation are shown in figures 6(b)–(e). Frame (b) shows the measured neutron evolution in red. The predicted neutron emission for a TRANSP run without fast-ion diffusion is shown in green, and clearly overestimates the emission while failing to capture the dynamics. The neutron emission from a TRANSP run with impulsive fast-ion diffusion is shown in blue. The diffusion in this case is that in frame (a) of the figure (radial width of 0.7 and amplitude of 50 $\rm m^2\,s^{-1}$, with 1 $\rm m^2\,s^{-1}$ between the bursts). As will be discussed below in greater detail, the value of 1 $\rm m^2\,s^{-1}$ between pulses is at the upper range of diffusivities that are likely for MHD-free periods. Note, however, that figure 5(a) shows a continuous $n = 1$ mode during the time of analysis ($0.4 < t(\rm sec) < 0.6$), which may explain the need for additional steady-state diffusion.

The plasma stored energy is shown in frame (c); here, the red trace is the 'fast' stored energy from a diamagnetic loop. The green curve shows the stored energy calculated by TRANSP with no impulsive fast-ion diffusion. This curve once again overestimates the measured values. The TRANSP calculation with impulsive fast-ion diffusivity (in red) is much closer to the measurement. Also interesting is the similar magnitude of the stored energy drops in the fast measurement and the TRANSP calculation with impulsive fast-ion diffusion.

Frame (c) also shows the $\rm D_\alpha$ emission from an outboard midplane viewing chord. Each bursting mode has an associated spike in this emission, likely associated with the loss of fast ions. Similarly, the fast-ion loss power computed by TRANSP is shown in frame (d). The case without impulsive diffusion shows a steady loss power of ~1.5 MW, while the case with impulsive diffusion has spikes up to 15 MW. Of course, one must remember that fast-ion loss modelled in TRANSP probably does not have the same energy and pitch angle dependence as that due to the actual modes. The frame is provided to show the level of transport associated with the events when these two variables are excluded.

Finally, the loop voltage is shown in frame (e). This voltage is determined by a feedback loop for maintaining constant plasma current. We observe that many modes trigger an increase in loop voltage from the control system, consistent with each mode ejecting a significant fraction of the current carrying fast ions.

Many scans of the impulsive fast-ion diffusion parameters were tested in order to develop the 'optimal' spatial and temporal profile shown in figure 6(a); some of these scans are shown in figure 7. As noted above, the main parameters to be optimized are the radial width of the region of large diffusivity (w in equation (3)), and the level of diffusivity in that region (peak values of $A_{\rm FI}$ in equation (3)). The measured neutron emission, with a band indicating the standard deviation of the signal within the averaging window, is shown in grey. The key criterion in selecting the optimal $D_{\rm FI}$ fit dynamics is that both the average value and typical time variation match the measurement.

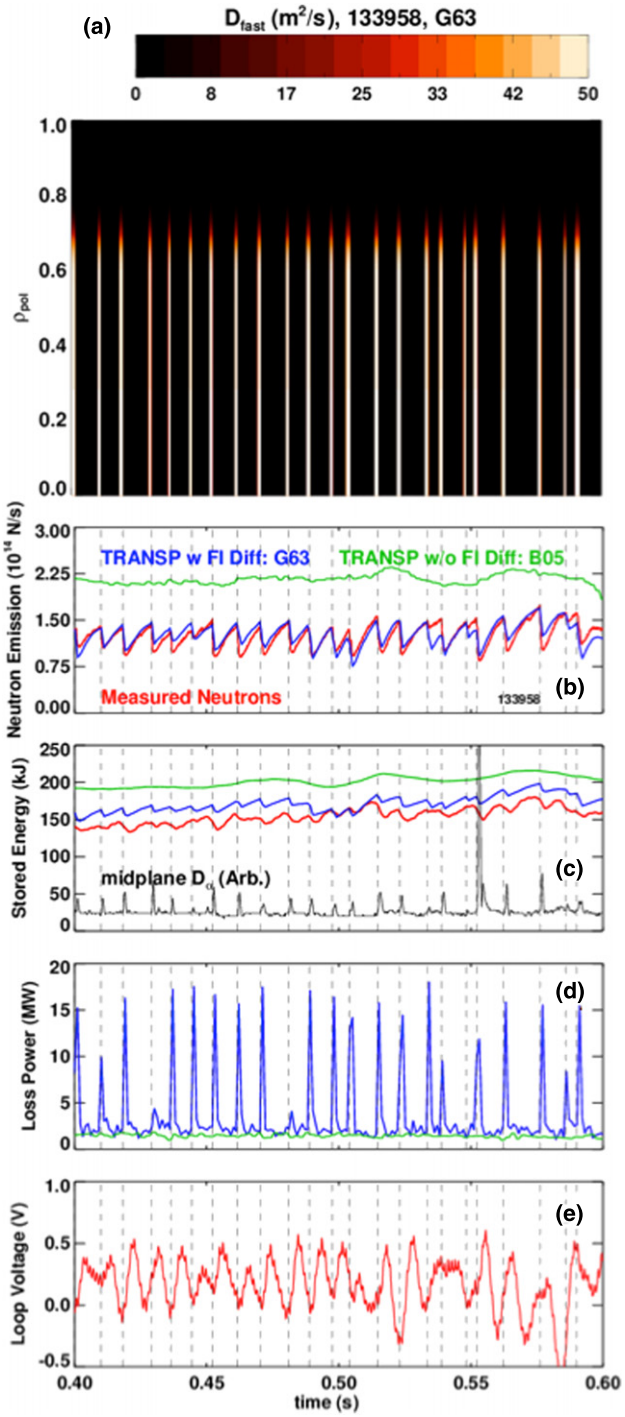

Figure 6. Simulation of the effects of TAE Avalanches using the TRANSP+NUBEAM code. The imposed fast-ion diffusion profile evolution is shown in frame (a). The time traces show (b) the neutron emission, (c) the stored energy (and midplane D_α emission), (d) the calculated fast-ion loss power and (e) the loop voltage. In each case, the measurement is indicated in red, a TRANSP simulation without fast-ion diffusion is shown in green and a TRANSP simulation with impulsive fast-ion diffusion is shown in blue.

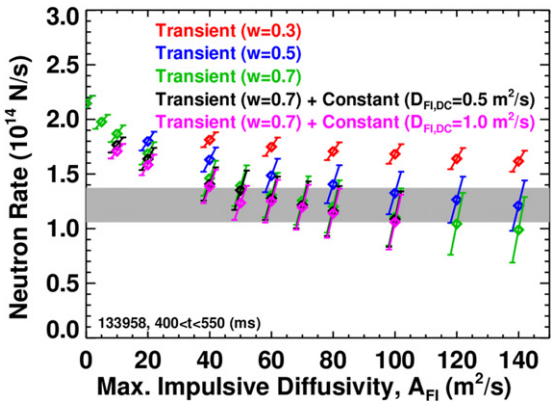

Figure 7. Comparison of the neutron emission as a function of the amplitude of the impulsive fast-ion diffusivity, for various assumptions about the profile width and diffusivity between bursts.

The red points show a scan of the impulsive diffusivity where the width of the diffusivity is limited by $w = 0.3$. It is impossible to increase the amplitude of the impulsive diffusivity enough to match the measured neutron emission. The blue points show a scan with radial width of the large-diffusivity region given by $w = 0.5$. The average neutron level can be matched in this case, assuming very large impulsive values of the diffusivity ($140\,\mathrm{m^2\,s^{-1}}$). However, the action of the modes is then too large, resulting in an overestimate of the signal variation (i.e. overestimation of the size of the neutron rate drops).

The simulation with the high-diffusivity region limited to $w = 0.7$ (green) can match the mean value with 60–80 $\mathrm{m^2\,s^{-1}}$ impulsive values, but also fails to match the variation. However, when 'small' levels of dc diffusivity are added between the pulses, excellent agreement can be reached in the both the magnitude and variation of the neutron rate. This case with $D_{\mathrm{FI}} = 1\,\mathrm{m^2\,s^{-1}}$ between modes and spiking to $50\,\mathrm{m^2\,s^{-1}}$ during the event results, already illustrated in figures 6(*b*) and (*c*), in a good match to both the typical crash amplitude and recovery rate after a crash.

We turn now to the implication of these modes for the current profile reconstruction. Figure 8(*a*) shows the current profile constituents with purely classical calculations. The neutral beam current is shown in red, the bootstrap current in blue and the inductive current in magenta. The sum of these currents (plus the relevant component of the diamagnetic and Pfirsch–Schlueter currents) is shown in green in the figure. This green curve should be compared with the reconstructed current profile in black. Poor agreement is found between the two calculations, largely on account of the predicted large values of the central neutral beam current drive.

The situation is much improved when the neutral beam current drive is calculated including an impulsive fast-ion diffusivity; the diffusivity chosen in this case is the same as that in the blue traces in figures 6(*b*) and (*c*) and shown versus radius and time in figure 6(*a*). The only change in profiles for this case is the strong reduction in the beam current drive, which brings the central current density down to a value consistent with reconstructions. The various current fractions are $f_{\mathrm{Ind}} \approx 45\%$ (inductive), $f_{\mathrm{PD}} \approx 38\%$ (pressure driven) and $f_{\mathrm{NB}} \approx 15\%$ (neutral beam) for this case.

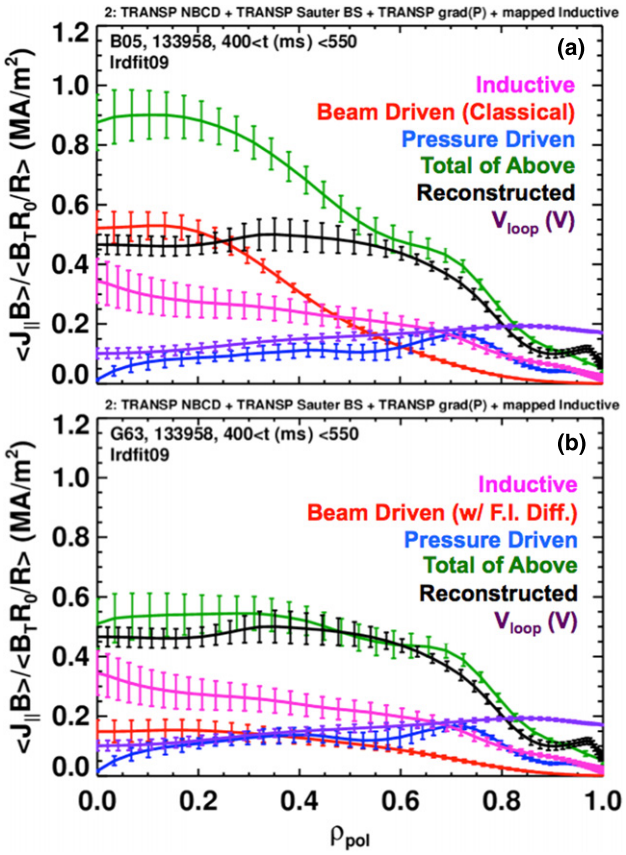

Figure 8. Comparison of the current profile reconstruction, using (*a*) classical collisional beam physics only and (*b*) the impulsive anomalous fast-ion diffusivity that matches the observed neutron rate modulations and stored energy.

4.2. *Continuous coupled $n = 1$ modes*

Next we turn to the discharge in black in figure 4, where a large $n = 1$ mode is visible in frame (*b*). The MHD mode spectrum for this discharge is shown in figure 5(*b*). A very complicated evolution of modes is observed early in the discharge, with a large series of chirping $n = 2$ and 3 modes, accompanied after 0.4 s by steadily rotating $n = 1$ modes. The chirping modes are largely eliminated by 0.55 s, and a large $n = 1$ mode, with higher-n harmonics, dominates the spectrum. The frequency of this mode is an excellent match to the rotation frequency of the $q = 2$ surface, as inferred from MSE-constrained reconstructions and the CHERS data and plotted in magenta. This confirms that the underlying mode will have an important $m/n = 2/1$ component.

Further information regarding the mode dynamics can be seen by examining the signals from a fan array of ultra-soft x-ray (USXR) signals [102]. The geometry of the array is illustrated in figure 9(*c*), and the data for this case are shown in figure 9(*a*). The signals have been band-pass filtered to include only content with $5\,\mathrm{kHz} < f < 20\,\mathrm{kHz}$. An inversion layer in the USXR emission is observable across chord 9; this chord is approximately tangent to the $q = 2$ surface radius, and indicates the presence of a magnetic island at this radius. There is also a strong inversion across the magnetic axis (chord 2), indicating the presence of an odd-m core localized mode.

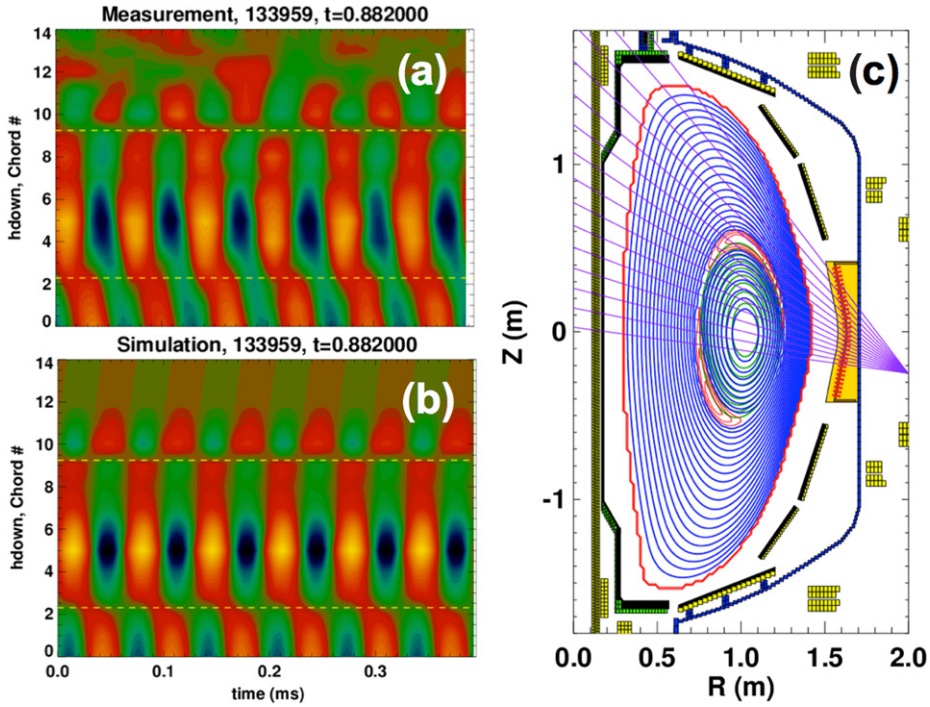

Figure 9. Comparison of the (*a*) measured and (*b*) modelled USXR emission for the case with a strong core $n = 1$ mode and (*c*) the model eigenfunction associated with the simulation. Chord #2 passes through the magnetic axis, while chord #9 is nearly tangent to the $q = 2$ surface.

We have been able to reproduce the most important features of this measurement using model eigenfuctions. The eigenfunction is composed of a 2/1 magnetic island coupled to a 1/1 core kink. The radial location of the island is determined by the radius of the $q = 2$ surface, and the width is an adjustable parameter. The core 1/1 kink is determined by a shift of the inner surfaces, where the magnitude of the shift and its radial extent are free parameters.

The free parameters are determined by the USXR data. The time- and chord-averaged emission is inverted to find $\varepsilon(\psi)$, the emission as a function of poloidal flux. Next, this emission is mapped to the eigenfunction. The emission is then integrated along the chords of the USXR array. This integration is then repeated for many phases of the eigenfunction with respect to the detector array, mimicking the effect of plasma rotation on the detected signal. More information on this analysis process can be found in appendix A.

The result of such a simulation is shown in figure 9(*b*), where the colour scale, though arbitrary, is the same for both frames (*a*) and (*b*). The most prominent features of the measured contours are clearly reproduced. These include the inversion across chord 9, indicative of the $m/n = 2/1$ island, and the inversion across the magnetic axis, indicative of the 1/1 kink. Furthermore, the fluctuation amplitude is the same in both the measurement and simulations.

The eigenfunction from this calculation is shown in figure 9(*c*), where the blue curves are the closed flux surfaces of the new perturbed equilibrium with the island and core kink. The magnetic islands are displayed in red. Also shown in green are the unperturbed magnetic surfaces inside the radius of the $q = 2$ surface. The displacement between the blue and green surfaces in the plasma core provides a sense of the amplitude of the displacement; the present simulation indicates a displacement of ∼2.5 cm is present for the core mode, and that the island width at the outboard midplane is ∼6–7 cm.

Comparison of the simulated and measured emission contours in figures 9(*a*) and (*b*) also reveals the limitations of the present model. Most strikingly, the data in frame (*a*) reveal that there may be an additional inversion layer outside the radius of the $q = 2$ island. This is likely an $m/n = 3/1$ magnetic island. Also, the somewhat different structure of the emission contours near the magnetic axis indicates that the simple $m/n = 1/1$ kink model may be insufficient to capture all the details of the actual mode.

We have again used the neutron emission to find fast-ion diffusivity profiles consistent with the data. As before, the $D_{\rm FI}$ profile was specified using equation (3) as a tanh profile of various widths and amplitude. All parameters were fixed in time for a given TRANSP calculation, but scanned in a series of independent TRANSP runs. Figure 10(*a*) shows that for zero anomalous diffusivity (the far left of the graph), the neutron emission is overestimated in TRANSP by a factor of ∼30%. Shown in red are the simulated neutron rates for a very narrow profile of the diffusivity ($w = 0.15$), where it is essentially impossible to match the measured emission except at very large diffusivity. However, for $D_{\rm FI}$ profile widths of $w = 0.3$, 0.45 and 0.6, it is possible to match the neutron emission using different values of the diffusivity magnitude. The $D_{\rm FI}$ profiles that allow a neutron rate match are shown in figure 10(*b*), where it is clear that it is possible to trade off profile width and amplitude in order to match the neutrons. Resulting neutral beam current drive profiles are shown in figure 10(*c*). It is clear that all three current drive profiles with $D_{\rm FI} > 0$ dramatically reduce the core beam current drive, but also that the three beam current drive profiles are largely indistinguishable from each other.

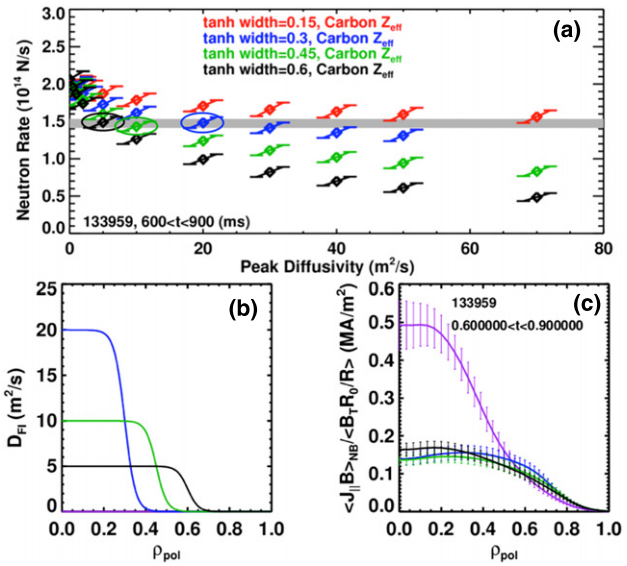

Figure 10. Study for the determination of the fast-ion diffusivity width and amplitude, for the discharge with coupled core $1/1 + 2/1$ modes. Shown in (a) are the measured neutron rate in grey, and the simulated neutron rate for a variety of diffusivity profiles and widths; the x-axis corresponds to the parameter $A_{\rm FI}$ in equation (3). Also shown are (b) the diffusivity $D_{\rm FI}(\rho_{\rm pol})$ and (c) the neutral beam current drive profiles, for a case without any anomalous diffusion (in purple), and three cases with diffusion to match the measured neutron rate. These three cases are circled in frame (a).

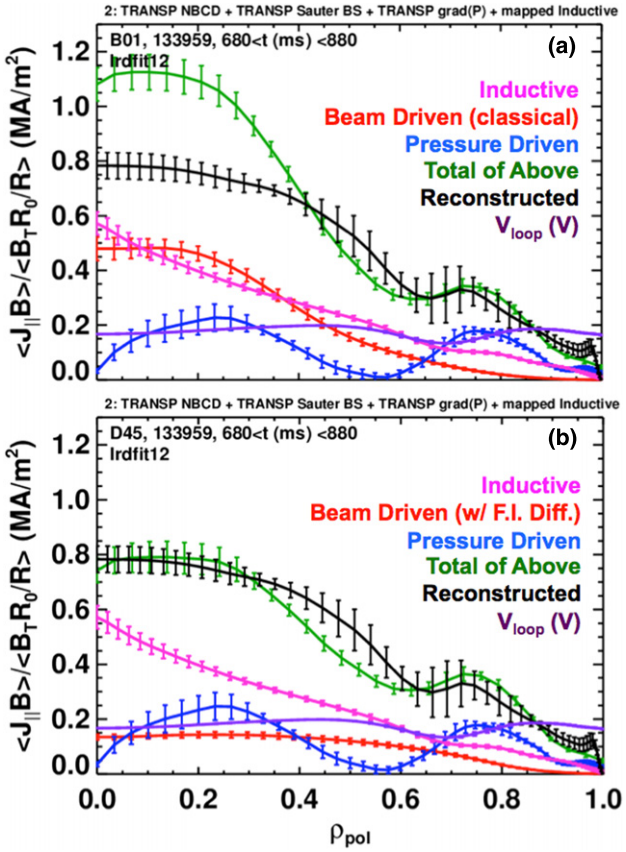

Figure 11. Calculation of the current profile for discharge 133959, (a) using classical beam processes and (b) including anomalous fast-ion radial diffusion.

Finally, the calculation of the current profile components is shown in figure 11(a), where the colour scheme is the same as used in figure 8. As with the previous case, the purely classical accounting for the current profile predicts excessive current near the magnetic axis, again due to the strong peaking of the neutral beam current. However, figure 11(b) shows that using the TRANSP run with a $D_{\rm FI}$ profile width of 0.45 and a diffusivity of $10\,{\rm m}^2\,{\rm s}^{-1}$ (these are the parameters of the green curves in figures 10(b) and (c)), the current profile accounting is much more accurate. Some discrepancy remains at $r/a = 0.5$; this is potentially due to the errors in the $n = 0$ profiles and equilibrium constraints due to the large rotating $n = 1$ perturbations. In this case, the various current fractions are $f_{\rm Ind} \approx 36\%$, $f_{\rm PD} \approx 39\%$ and $f_{\rm NB} \approx 17\%$. These sum to 92%, implying that the sum over independently calculated current sources does not totally add up to the known toroidal current. As discussed in section 8, one source of error is the somewhat lower current density at the plasma edge in the green curve, compared with the reconstruction in black.

There have been a number of studies of core $n = 1$ kink and tearing modes in NSTX H-mode plasmas. The first large study of $n = 1$ core kink modes was published in [103]. It was shown there that these modes can cause severe rotation damping and degrade fast-ion confinement. These studies were extended to understand the effect of the modes on the current profile in [67, 68]. That reference illustrated that these core $m/n = 1/1$ modes can cause significant fast-ion current redistribution. A study of the neoclassical aspects of $m/n = 2/1$ islands in NSTX was published in [104], demonstrating that multiple mechanisms can trigger these modes; cases were illustrated with energetic particle mode (EPM) triggers, ELM triggers and 'triggerless' mode strikes. It was also shown that the rotation shear at the $q = 2$ magnetic surface was an important variable for determining the threshold neoclassical drive for striking the modes, a result also found in DIII-D [105–107]. Saturated core $n = 1$ modes have also been observed in MAST [108].

Reference [104] also described, but did not show in a figure, that the 2/1 modes are typically coupled to 1/1 core modes. This result is actually not uncommon, as the coupling of m/n neoclassical tearing modes to $m - 1/n$ core kinks has been documented in TFTR [109] and ASDEX-Upgrade [110] and predicted by theory [111]. Indeed, the destabilization of the 2/1 mode without an obvious trigger in [104] may be due to the $m/n = 1/1$ mode providing the initial instability drive. The conditions under which either the 2/1 or 1/1 component dominates the triggering and saturation process in NSTX is not fully understood, and is the subject of continued study.

With respect to the redistribution of the neutral beam current, it is likely that both the central 1/1 mode and the higher-m islands play an important role. In general, it has been found that quasi-static magnetic perturbations produce islands in the phase-space trajectories of energetic ions [112]. A single magnetic perturbation can cause multiple phase-space islands due to the coupling between the $m = 1$ structure of the magnetic drifts and the magnetic perturbation. These drift islands themselves can enhance the fast-ion transport; however, when they overlap, the transport is significantly increased. This overlap condition then sets the threshold for stochastic fast-ion transport. If multiple-helicity magnetic

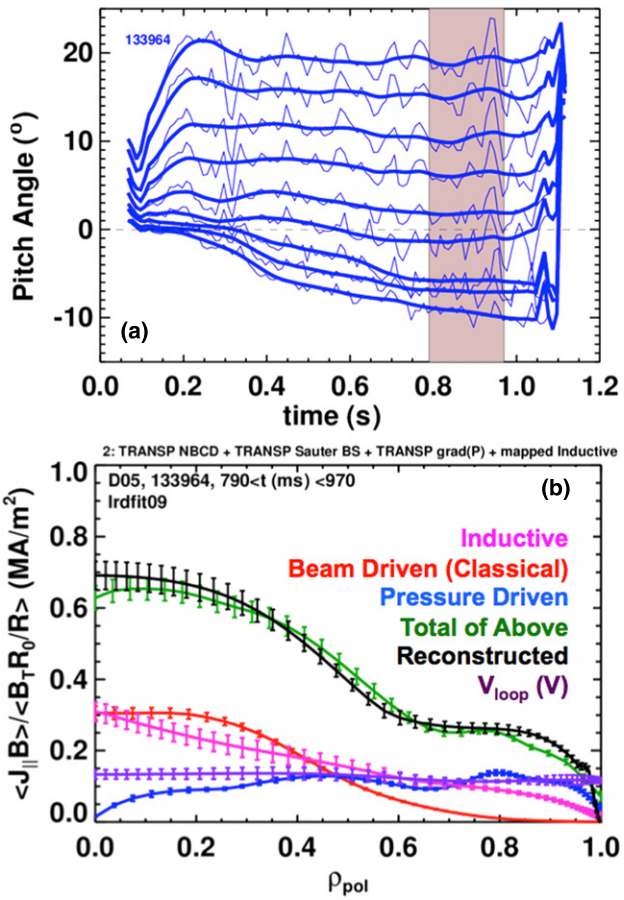

Figure 12. Pitch angles (*a*) and current profile accounting (*b*) for the blue discharge in figure 4. The direct pitch angle data, in thin lines, have been smoothed with a 100 ms time constant to produce the thick lines, in order to emphasize the slower evolution. This discharge achieved the lowest ever flat-top average loop voltage for a beam heated H-mode discharge.

perturbations are present, the threshold magnetic perturbation for stochastic transport can be reduced [112]. This explanation has been successfully applied to model fast-ion loss due to low-frequency MHD in DIII-D [42], TFTR [113] and ASDEX-Upgrade [60–62, 114]. The large mode amplitudes and multiple-harmonics make this explanation quite plausible for the present case. The detailed interaction of the fast ions with the complex magnetic perturbation is, however, out of scope for this paper, and is a topic for future study.

4.3. Discharge free of low frequency MHD

The final discharge in the 0.7 MA, 0.48 T study, shot 133964, had a long MHD-free period. This achieved the lowest ever flat-top average loop voltage (130 mV) for a long-pulse NSTX H-mode discharge. The magnetic field pitch angle evolution for this discharge is shown in figure 12(*a*), and illustrates that a nearly fully evolved current profile is achieved by the end of the discharge. The grey area in this figure indicates the time during which the current profile analysis is executed.

The current profile analysis is shown in figure 12(*b*). The current profile accounting works quite well with no anomalous diffusion. The only large discrepancy occurs near the plasma edge, a common feature in this analysis that will be discussed

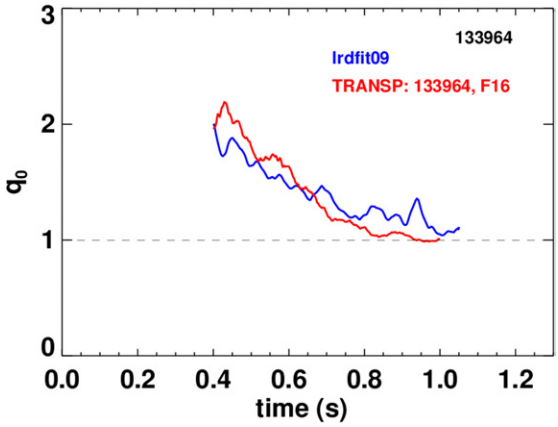

Figure 13. Comparison of the q_0 evolution from MSE-constrained reconstructions (blue), and from a poloidal field diffusion calculation using TRANSP (red).

in section 8. Note that the loop-voltage profile is quite flat, indicating that any further evolution of the current profile is quite small. The total non-inductive fraction is 62–68% in the discharge, with $f_{\rm Ind} \approx 33\%$, $f_{\rm PD} \approx 49\%$ and $f_{\rm NB} \approx 14\%$.

We have also used this discharge to compute the expected q_0 evolution by solving the poloidal field diffusion equation in TRANSP using the measured plasma profiles and reconstructed boundary shape. The poloidal field diffusion solver was turned on at $t = 0.4$ s, after most of the early MHD activity had subsided, and no anomalous diffusion of the beam particles is included in the simulation. The result of this calculation is shown in figure 13. Considering the equilibrated state towards the end of the discharge, the value of q_0 calculated by TRANSP is within 0.1 units of that derived from MSE-constrained equilibrium reconstructions. This calculation shows again that the neoclassical calculation of the current profile agrees reasonably well with the reconstruction. It should be noted, however, that this does not validate use of the TRANSP poloidal field diffusion solver with purely neoclassical physics for all time-dependent simulations. In particular, Alfvenic and tearing activity during and just after the current ramp-up is quite common. Given the results of this section, it appears that this mode activity will almost surely modify the current profile evolution.

5. Current profile reconstructions in moderate-q_{95} plasmas optimized for long pulse

The second class of discharges selected for study were optimized for long-pulse operations. This requires that the magnitude of the toroidal field be reduced so that the coil heating limit is reached later in the discharge. The task is then to optimize the discharge parameters such that the current limit on the solenoid and heating limit on the toriodal field coil are reached simultaneously. The cases described here meet this criterion with $I_{\rm P} = 0.7$ MA and $B_{\rm T} = 0.37$ T, with $q_{95} = 11$. We also note that a discharge subject to a similar optimization, and which lasted ~300 ms longer than those described here, was reported in [78].

Two example discharges from this set are shown in figure 14. The plasma current is displayed in frame (*a*);

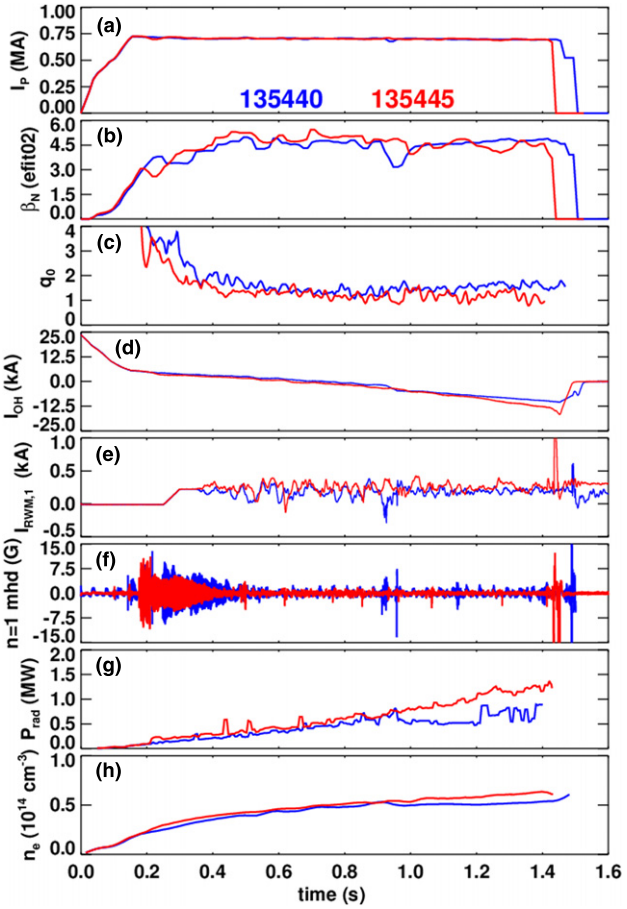

Figure 14. Time traces of two discharges designed to maximize the achievable pulse length in NSTX. Shown are (*a*) the plasma current, (*b*) β_N, (*c*) the safety factor on axis (q_0), (*d*) the solenoid current, (*e*) the current in a representative RWM coil, (*f*) the $n = 1$ rotating MHD signal, (*g*) the radiated power and (*h*) the line-average density.

these discharges have pulse lengths in excess of 1.5 s. The β_N evolution is shown in frame (*b*), with values of ∼5 common in these cases. Note the transient reduction in β_N at approximately 0.9 s in the blue trace, (discharge 135440), apparently due to a very large edge localized mode (ELM); as will be seen below, this transient leads to transition in the profiles, and development of a more quiescent plasma configuration. The reconstructed central safety factor is shown in frame (*c*), and saturates above unity for both discharges in this study, indicating that the current profiles have stopped evolving. The solenoid current is shown in frame (*d*). The two discharges have very similar flux consumption until the event in 135440; that discharge then uses flux at a somewhat lower rate. The current in a representative RWM coil is shown in frame (*e*). The fluctuations in this signal are due to the $n = 1$ mode feedback system [80, 81], and the reduction in the fluctuation amplitude after $t = 0.8$ s in 135440 is further indicative of the transition to the quiescent regime.

This interesting quiescent regime has additional desirable features. The volume integrated radiated power is shown in frame (*f*). The discharge without the quiescent transition shows a continuous ramp of the radiated power, as is typical of discharges with lithium conditioning. However, the radiated power rise is arrested after the quiescent-regime transition in

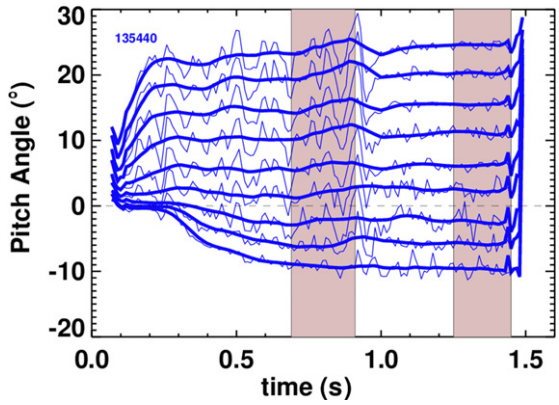

Figure 15. Pitch angle evolution for shot 135440, the blue discharge in figure 14. The dark bands indicate the time windows for averaging in subsequent plots. Thin traces are the direct pitch angle data, while thick traces have a 100 ms smoothing filter applied in order to emphasize the slow evolution.

135440. The density rise in frame (*g*) is also stopped. This discharge has thus stopped evolving in both the current and the kinetic profiles. No large rotating MHD activity (frame (*h*)) is visible once the transient modes at the beginning of the discharge die away.

That these discharges reach a fully evolved current profile is illustrated not only by the q_0 evolution in figure 14(*c*), but also in the magnetic field pitch angle evolution shown in figure 15. The traces shown are for discharge 135440 in blue above, which has the MHD event/ELM at $t \sim 0.9$ s followed by transition to the more quiescent state. Note that the pitch angles have largely stopped evolving by ∼0.7 s. After the ELM at ∼0.9 s, the deviation in time of the pitch angles is much reduced, providing additional evidence of the quiescence of the new configuration; any further pitch angle evolution is arrested by ∼1.25 s. The shaded areas in the figure indicate the times for subsequent kinetic and current profile analysis.

The kinetic profiles for discharge 135440 are shown in figure 16. The blue traces show the profiles before the ELM driving the transition to the new quiescent regime, while the black profiles are taken from after the transition. We see that, after that transition, the electron density decreases at the edge but increases in the core, while the deuterium density increases across the profile. This latter is the expected result when the impurities are flushed from the discharge, followed by a period without impurity accumulation. Note the local reduction in density gradient near $\rho_{pol} = 0.8$ after the transition. This feature is also observed in the electron temperature after the transition, where the central electron temperature is slightly lower, but a larger drop occurs in the edge region $\rho_{pol} > 0.8$.

We have applied these current profile reconstruction techniques to these discharges, and, as shown in figure 17, have found good agreement between the reconstructed current profile and that computed by summing the components. No fast-ion diffusivity is used in these calculations. The current comparison before the confinement transition is shown in figure 17(*a*), and looks quite similar to the higher q_{95} case in figure 12(*b*). The current profile after the transition shows less current at the plasma edge, for both the reconstructed case and the constituent sum. This is due to the relaxation of the edge pressure gradient noted above, leading to a reduction in

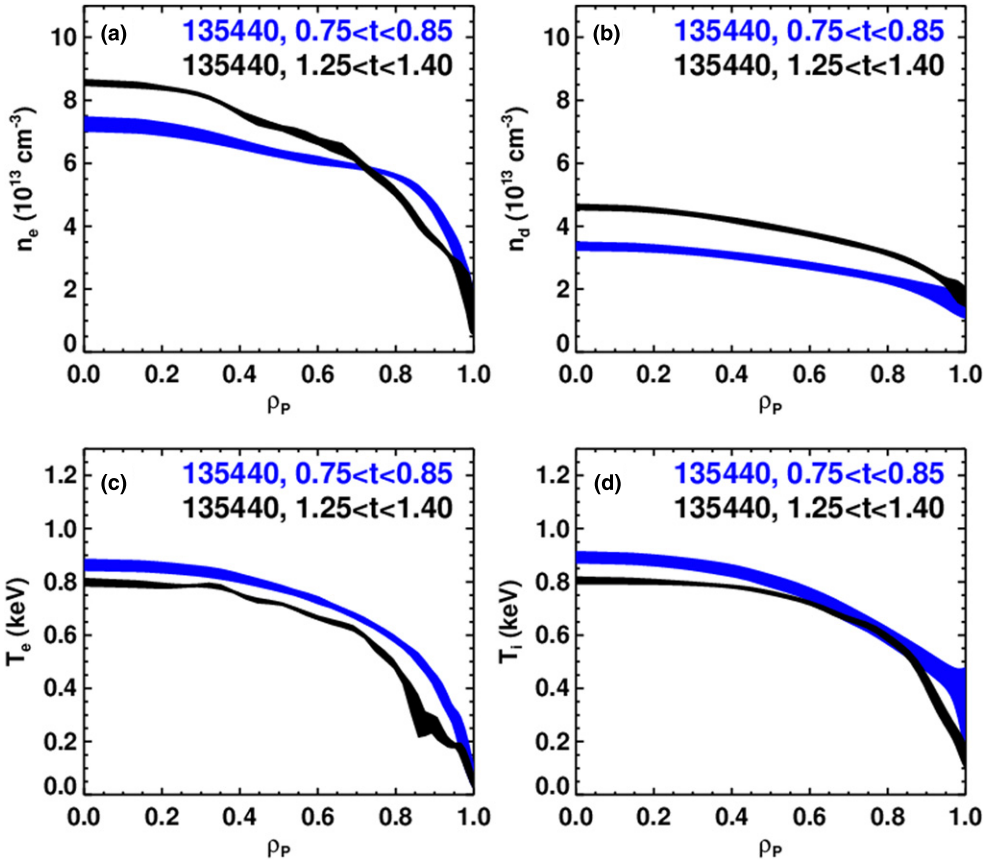

Figure 16. Mapped kinetic profiles before and after the transition to the more quiescent conditions in discharge 135440. Shown are profiles of the (*a*) the electron density profiles, (*b*) the deuterium density, (*c*) the electron temperature and (*d*) the ion temperature.

the bootstrap current in that region. In both cases, the loop-voltage profile is flat, again implying that the current profile has stopped evolving. The non-inductive fractions for the two time windows are $f_{\rm Ind} \approx [41, 37]\%$, $f_{\rm PD} \approx [45, 49]\%$ and $f_{\rm NB} \approx [10, 8]\%$, where the discrepancies with respect to 100% are mostly due to the inability of the constituent sum to perfectly match the reconstructed current density at the plasma edge.

6. Current profile reconstructions in low-q_{95} plasmas optimized for high stored energy and high $\beta_{\rm T}$

The final set of discharges considered here are higher current cases, designed to maximize the sustainable toroidal beta or stored energy. These goals are typically met by increasing the plasma current and operating at reduced q_{95}. The maximum pulse duration is then determined by the flux consumption and solenoid current limit.

Time traces from example discharges are shown in figure 18. The plasma current from these three cases is shown in frame (*a*), illustrating that these examples have 1 MA, 1.1 MA and 1.3 MA of plasma current. The first two cases were run with a toroidal field of 0.45 T, while the 1.3 MA case was run with $B_{\rm T} = 0.48$ T. The $\beta_{\rm N}$ evolution in frame (*b*) shows that all cases reach $\beta_{\rm N}$ in excess of 5. This corresponds to 430 kJ for the 1.3 MA plasma, which is close to the NSTX record of 460 kJ. The evolution of the central safety factor is shown in (*c*), and it is clear that none of these cases have reached a stationary state by the end of the discharge. The internal inductance ($l_{\rm i}$) is shown in frame (*d*). This class of plasmas has among the lowest values of $l_{\rm i}$ in all beam heated discharges in NSTX, with $\beta_{\rm N}/l_{\rm i}$ ratios up to 13.5 achieved. Indeed, the reduction in the $I_{\rm P}$ ramp rate in 135117 (the red discharge) was implemented in an attempt to avoid such low $l_{\rm i}$ levels. The solenoid flux is shown in frame (*e*), and the odd-n low-frequency MHD in frame (*f*). The 1.1 MA case in red develops a rotating $n = 1$ MHD mode at $t = 0.95$, after which the slope of the solenoid current increases to a high rate to provide additional loop voltage. Otherwise, the flux consumption essentially follows the plasma current level. Each discharge has a >100 ms period during which there is very little MHD activity. The calculations presented below for these discharges are done during this MHD-free window and do not use any anomalous fast-ion diffusivity.

The current profile reconstruction for these three cases is shown in figure 19. We see that as before, the current profile accounting generally works well: the green and black curves are in reasonable agreement for all three cases. There are some significant differences between these cases and those discussed previously. Most importantly, the loop-voltage profiles for these cases are all hollow on average, indicating that the current profile has not yet come into equilibrium at these higher values of plasma current.

It was noted above that these plasmas tend to have lower values of the internal inductance $l_{\rm i}$ compared with those at lower current. This can be seen in the current profiles below,

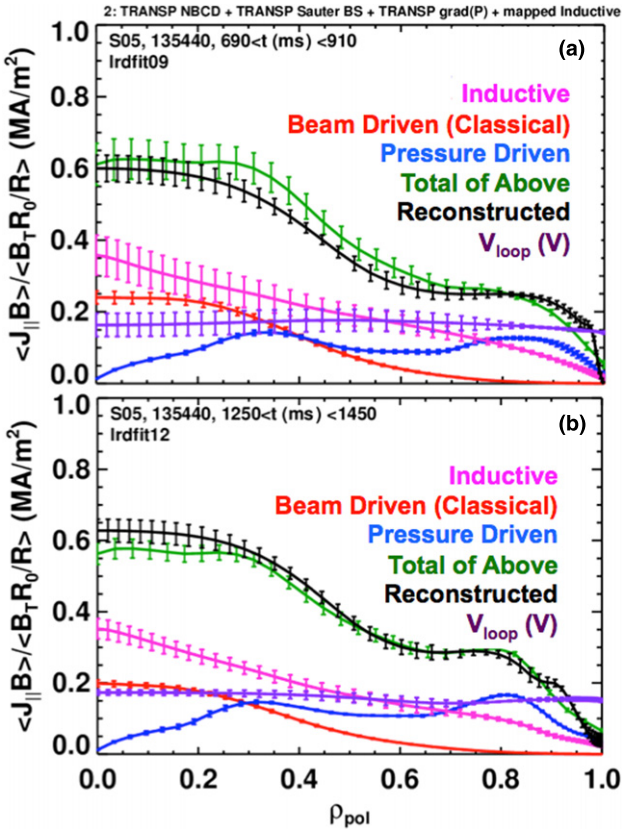

Figure 17. Reconstruction of the current profiles for long-pulse discharge 135440. The profiles are for times (*a*) before and (*b*) after the change to the more quiescent configuration.

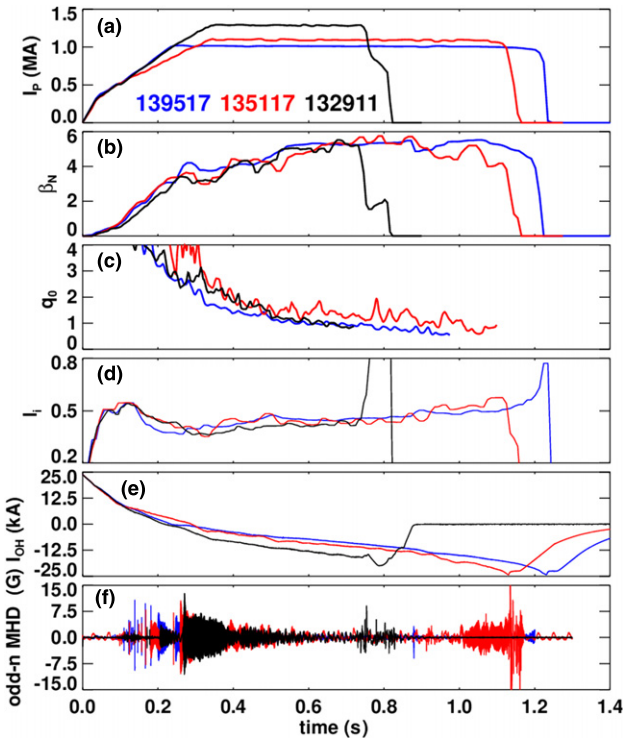

Figure 18. Time traces of high-current discharges designed to maximize the stored energy (132911), and the sustainable value of β_T (135117 and 139517).

where, for instance, the current density at the top of the pedestal ($\rho_{pol} \sim 0.8$) is a larger fraction of the central current density than for the lower current cases in figures 12(*b*) and 17. Of course, these current profiles are not fully relaxed, and the central current would be larger once the loop-voltage profiled flattened and the conductivity was allowed to determine the current density. These cases with plasma currents of [1.0, 1.1, 1.3] MA have current fractions of $f_{Ind} \approx [48, 44, 52]\%$, $f_{PD} \approx [38, 38, 35]\%$ and $f_{NB} \approx [9, 6, 7]\%$, with the unaccounted for current occurring at the edge.

7. Upper bounds of the fast-ion diffusivity in MHD-free discharges

As noted in section 1, some previous studies of neutral beam current drive have invoked a small amount of anomalous fast-ion diffusion, even in the absence of low-frequency MHD activity. In ASDEX-Upgrade experiments with off-axis NBCD, a diffusion coefficient of $0.5\,m^2\,s^{-1}$ was used to enable the fast-ion current to fill in on axis, yielding better agreement with the measured pitch angle evolution; this additional diffusivity was attributed to turbulent transport [60]. Experiments in DIII-D [48–50] found that the neutron emission, neutral beam current drive and the FIDA spectrum are typically consistent with TRANSP calculations including classical processes only. The exception to this is the high injected power regime with small E/T (where E is the injected fast-ion energy and T is the plasma temperature), where an anomalous fast-ion diffusivity was also invoked; a threshold depending on E/T is consistent with some expectations from electrostatic turbulence [115, 116]. Note that with injected ions in the 70–90 kV range and temperatures of ~1 keV in neutral beam heated discharges, the E/T values in NSTX are much higher than the threshold values in the DIII-D studies.

The calculations presented in sections 3–6 show that in the absence of low-frequency MHD, NSTX results can be understood without invoking additional anomalous fast-ion diffusion. However, this observation does not eliminate the possibility that some small level of anomalous fast-ion diffusion may be present, and it is interesting to study whether the data can provide an upper bound on D_{FI} in these MHD-free discharges.

We begin to assess this question by looking at simulations of high-q_{95}, high-β_P discharge 133964, studied in figure 12 and high-β_T discharge 135117, shown in figure 19(*b*). We have run the TRANSP+NUBEAM code with various levels of fast-ion diffusion, leaving all other input options fixed. The diffusion in this case is a constant in both space and time. Considering the neutron emission in figure 20, it appears that fast-ion diffusivities in the range of $0 < D_{FI}\ (m^2\,s^{-1}) < 2$ are essentially consistent with the measurement for 133964 in frame (*a*), and up to $4\,m^2\,s^{-1}$ for 135117 in frame (*b*). The on-axis current density is more sensitive than the neutrons to the diffusivity, with $D_{FI} = 1\,m^2\,s^{-1}$ resulting in a ~20% reduction in the current density for both cases. This is essentially the highest value of D_{FI} (and current density reduction) consistent with the profiles in figures 12 and 19(*b*).

Using the neutron rate to bound the possible fast-ion diffusivity is subject to error if the absolute calibration on the

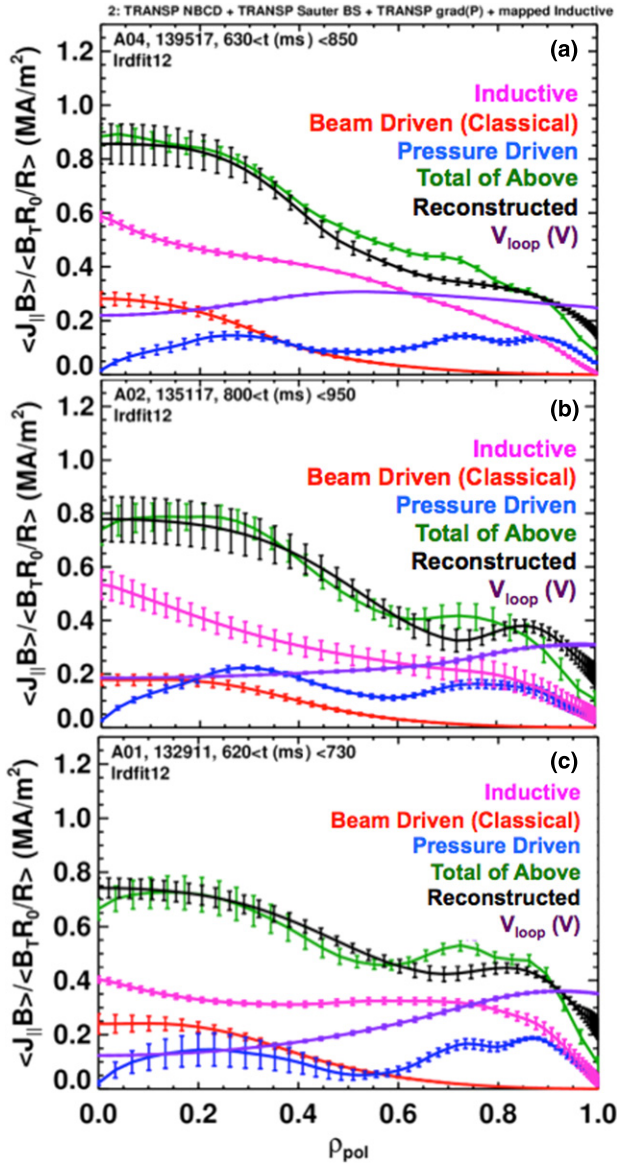

Figure 19. Current profile reconstructions for the three discharges in figure 18. These cases have (*a*) 1.0 MA at q_{95} of 8, (*b*) 1.1 MA at q_{95} of 8 and (*c*) 1.3 MA at q_{95} of 7.5.

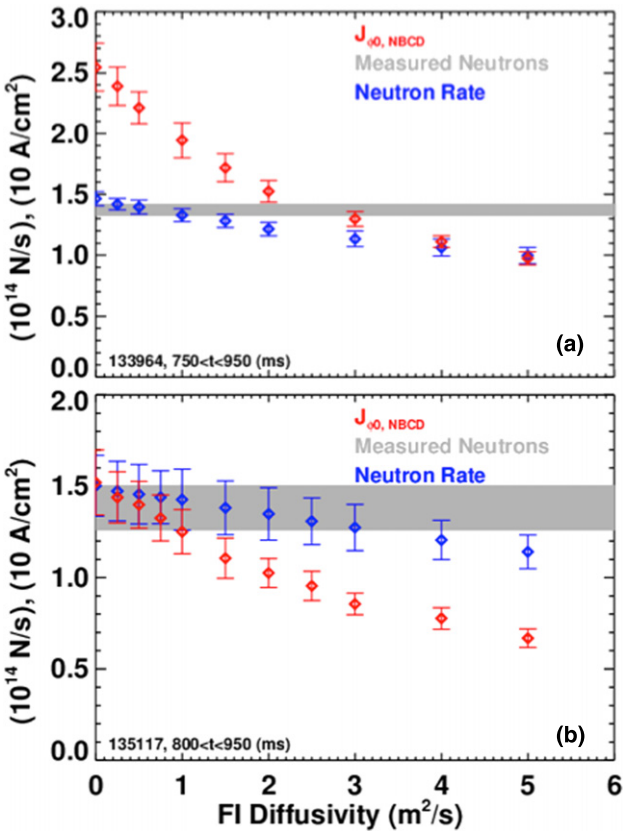

Figure 20. The predicted neutron rate and central neutral beam toroidal current density, as a function of the imposed fast-ion diffusivity. The grey line indicates the measured neutron emission rate, including the statistical variation of the signal within the averaging window. The shots shown are (*a*) a 0.7 MA high-β_P shot (133964) and (*b*) a 1.1 MA high-β_T discharge (135117).

detector is erroneous. The time-scale analysis described in section 3 can be used to eliminate uncertainties in this regard, as shown in figure 21. Frame (*a*) shows the simulated decay time (τ_D) of the neutron emission as a function of fast-ion diffusivity, while frame (*b*) shows the rise time (τ_R), for the same discharges as were studied in figure 2. D_{FI} is a constant in both space and time for these simulations. As with the neutron emission rate itself, the simulated decay time is largely insensitive to values of $0 < D_{FI}$ ($m^2\,s^{-1}$) < 0.5. However, larger values of fast-ion diffusivity, say, $>2\,m^2\,s^{-1}$ appear to be excluded by this analysis.

Beyond the possibility for turbulent diffusion of fast ions noted above, high-frequency Alfvenic activity in NSTX [97, 117–119] could also provide a mechanism for the transport of fast ions, in either physical or velocity space. An example of this activity is shown in figure 22, where the spectrogram for the high-β_P shot 133964 is shown; the neoclassical accounting of the current profile in figure 12 worked out cleanly in this case. While, as noted above, there is no low-frequency MHD activity, there remains considerable high-frequency activity. These modes have been identified as global and compressional Alfvén eigenmodes (GAEs and CAEs). There is some evidence that these modes may contribute to electron transport in NSTX [120], and the suggestion that they may provide a mechanism for the fast ions to directly heat thermal ions [121]. The study of these high-frequency CAE/GAE modes, and their impact on the global plasma performance, is an active part of the NSTX research program.

8. Discussion and summary

This paper has presented a systematic analysis of the current profile in NSTX high-performance NB heated H-modes, with a goal of establishing when standard neoclassical calculations of the current profile are experimentally justified. Under the conditions studied in this paper, we have found that:

- The neoclassical picture generally holds when low-frequency MHD is absent. This has been established over a range of q_{95} in high-elongation, high-performance NB heated plasmas.
- The neoclassical calculation generally fails when low-frequency MHD modes are present. Examples given

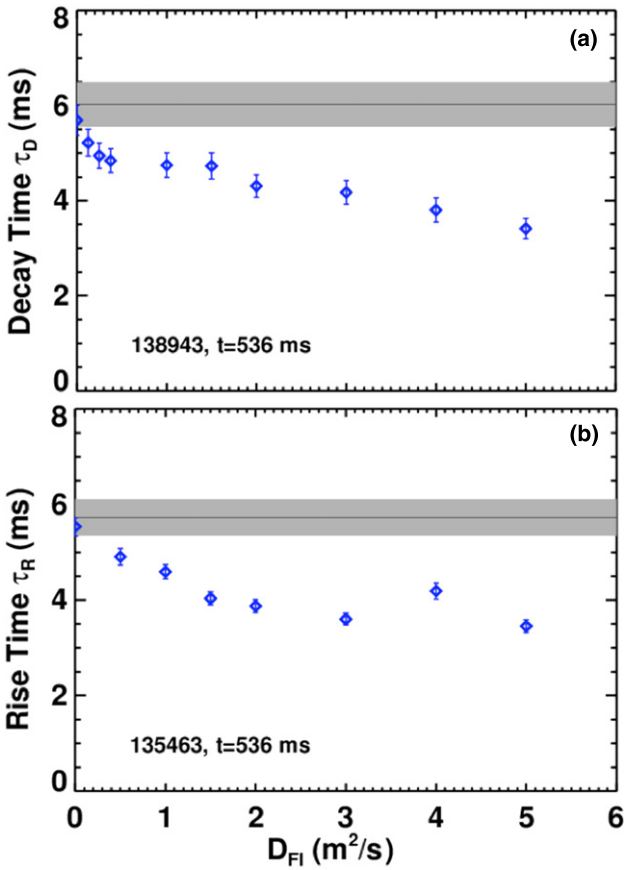

Figure 21. Calculation of the (*a*) rise and (*b*) decay time constants, as a function of the applied fast-ion diffusivity, for the two discharges shown in figure 2. Diffusivities up to $D_{\rm FI} \sim 0.5\,{\rm m}^2\,{\rm s}^{-1}$ are difficult to exclude based on these data.

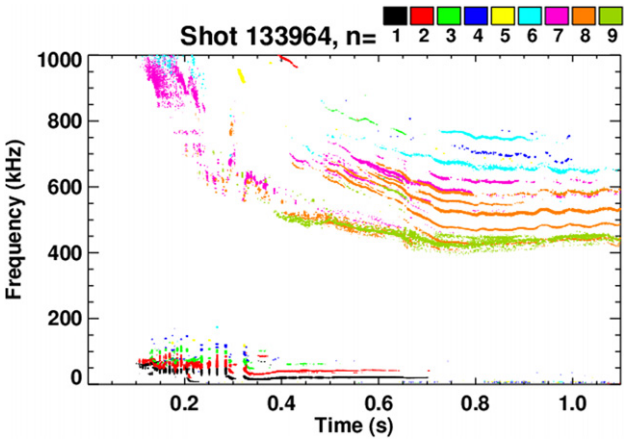

Figure 22. Spectrograms of the MHD activity for high-$\beta_{\rm P}$ discharge 133964. Many high-frequency modes can be identified during the phase of the successful current profile analysis ($800 < t < 1000$ ms).

here include TAE avalanches, and large coupled $m/n = 1/1 + 2/1$ modes. Agreement can generally be recovered in these cases when an anomalous fast-ion diffusivity is invoked.

- There is an upper bound of $\sim$ 1–2 $\rm m^2\,s^{-1}$ on the fast-ion diffusivity in MHD-free discharges.

Neoclassical calculations of this sort are often used to predict the ramp-up characteristics and steady-state current profile for the purpose of device design. The results in this paper are mildly encouraging, in that the stationary profile predictions using only neoclassical physics appears justified in the absence of low-frequency MHD.

However, as noted in [37] with respect to tearing modes, the assumption of neoclassical neutral beam current drive to ramp-up the plasma current may be questionable, given that these would likely be low(er) density plasmas with substantial fast-ion beta, a condition that is conducive to fast-particle driven MHD. Indeed, the ramp-up phase of most NSTX H-mode discharges has considerable fast-particle MHD. The conclusive prediction of the onset regime for these modes, and the fast-ion transport they cause, is a subject of continued research.

In addition to these observations regarding the current profile, a number of interesting plasma conditions have been observed. These include:

- Discharges that maintain 65–70% non-inductive fraction for many current redistribution times ($\tau_{\rm CR} \sim 300$ ms), without strong MHD activity. These are an improvement on the discharge noted in [67, 68], where the high non-inductive fraction phase is terminated by core $n = 1$ modes.
- An interesting example where a modification to the plasma profiles after an MHD event leads to an improved 'quiescent' configuration.
- Cases that have reached a fully evolved current profile.
- Use of USXR data to determine the structure of a coupled $m/n = 2/1$ magnetic island and 1/1 core kink.

Section 7 showed that the NSTX data in MHD-free cases are consistent with a small value of fast-ion diffusivity. While these small values have a minimal effect on the beam current drive for the present discharges, devices configured for substantial off-axis current drive may be more heavily impacted (the actual effect of the turbulence or high-frequency MHD modes may not be strictly diffusive, but we treat it that way here for convenience). This is illustrated by an example calculation in figure 23, where the driven current profiles for a single 90 kV, 2 MW deuterium source are shown for three different tangency radii ($R_{\rm tan}$) and five values of the spatially and temporally constant fast-ion diffusivity. The target discharge is the 1.1 MA case shown in figure 19(*b*), where the magnetic axis is at $R_{\rm maxis} = 105$ cm. The $R_{\rm tan} = 70$ cm case in frame (*a*) is essentially similar to the present NSTX source A, with a broad driven current profile. Increasing the fast-ion diffusivity to $0.5\,{\rm m}^2\,{\rm s}^{-1}$ causes a $\sim$13% drop in the central beam current density. For the $R_{\rm tan} = 100$ cm calculation in (*b*), the net current drive is significantly higher, and the effect of $0.5\,{\rm m}^2\,{\rm s}^{-1}$ is to reduce the central beam current density by $\sim$22%. Note, however, that as $D_{\rm FI}$ is increased, the total current remains unchanged, and the current density profile becomes broader, but without a profound change in the radial structure.

The situation is qualitatively different for the $R_{\rm tan} = 130$ cm case. The driven current peak with $D_{\rm FI} = 0$ is located significantly off axis, resulting in a very hollow profile. The inclusion of $D_{\rm FI} = 0.5\,{\rm m}^2\,{\rm s}^{-1}$ results in a 50% increase in

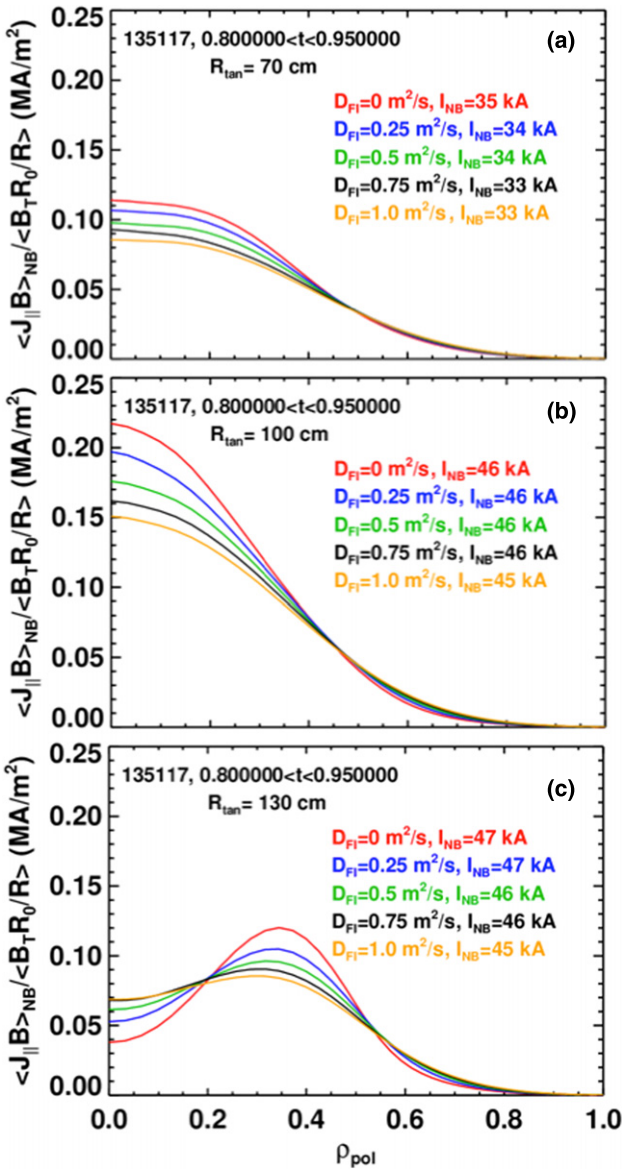

Figure 23. Predicted neutral beam current drive profiles as a function of fast-ion diffusivity, using the profiles from 1.1 MA shot 135117, for beam tangency radius of (*a*) 70 cm, (*b*) 100 cm and (*c*) 130 cm. The diffusivity is constant in space and time.

the central current density and a 25% decrease in the off-axis peak amplitude; the net effect is to fill in the hollow profile. The utility of the beam for $q_{\min}$ control would thus be partially compromised, though, for the flat $D_{\rm FI}$ profiles used here, the fast-ion total current is not changed. Hence, further experiments to resolve small levels of anomalous fast-ion transport are important. It is important to note that the details of this calculation would change in response to the changes in the plasma current magnitude and profile, changes in the kinetic profiles, or additional charge exchange loss. However, the spirit of the calculation, that off-axis current drive may be more sensitive to small amounts of fast-ion diffusion, remains. Note that a similar conclusion was drawn for ASDEX-Upgrade in [60], and observed in [47, 48, 65].

With regard to prediction of the current profile for next step-devices, the fact remains that although anomalous fast-ion diffusion may (or may not) be present, anomalous diffusion of thermal plasma particles, momentum, and heat remains an unsolved problem. In particular, the bootstrap current depends sensitively on the density and temperature gradients, which must be predicted based on models of the sources and sinks of particles and energy. Integrated modelling of conventional aspect ratio devices (see, for instance, [56] or [44]) have typically used reduced transport models such as GLF23 [122]. However, it remains unclear that these models can accurately represent the transport in a spherical torus, and this remains an area of active research [123]. We also note that since the particle and energy transport can respond to changes in the current density and magnetic shear, it is ultimately necessary to solve for all profiles self-consistently.

It is also worth noting a few sources of systematic error in the calculations presented above. The largest discrepancy between the reconstructed and 'summed' current profile is typically at the very edge of the plasma. Given that this region is heavily weighted in the area integral that determines the total current, a small error there can result in a large error in the total toroidal current. We have found that the reconstruction of the current profile in this region is quite sensitive to the basis functions used in the parametrization of $p'(\psi)$ and $ff'(\psi)$; it is desirable to provide sufficient freedom in the profiles to fit the data, consistent with time-slice to time-slice similarity of the reconstructions (in order to provide a smooth evolution of the poloidal flux for the loop-voltage calculation). The calculations here attempt to balance these constraints. We find, however, that our best effort reconstructions tend to produce larger current densities in that region than can be accounted for by summing the pressure-driven and inductive currents (the neutral beam driven current is predicted to be quite small at this radius). It is possible that a different parametrization of the edge profiles in the reconstruction code could help resolve this discrepancy. Alternatively, refined models of the bootstrap current, especially at the plasma edge, may be important.

A second systematic error could arise from centrifugal effects. The carbon density in NSTX is measured at the outboard midplane; it is then typically assumed that the densities measured there are indicative of all other points on the magnetic surface. However, centrifugal effects will lead the carbon to accumulate on the outboard midplane, causing this analysis to overestimate the global carbon density and inventory.

In order to correct for this effect, we have applied a centrifugal correction to the data, using methods described in [124] and previously applied to NSTX in [101]. First, the outboard midplane (OMP) values of the carbon and electron density are computed as a function of poloidal flux. These densities, and deuterium from quasi-neutrality, are then mapped around the magnetic surface by iteratively solving the quasi-neutrality constraint and the expression for the poloidal distribution of density for each species [124]:

$$n_j(\theta) = n_{j,\rm OMP}\ \exp\left(\frac{\frac{1}{2}m_j\omega^2(R(\theta)-R_0^2) - eZ_j\varphi(\theta)}{T_j}\right) \quad (4)$$

for all species; the outcome of the calculation is the poloidal electric field $\varphi(\theta)$. Here, θ is the poloidal angle, j is an index over the three species and the iteration was started with equation (9) of [124]. Note also that the deuterium

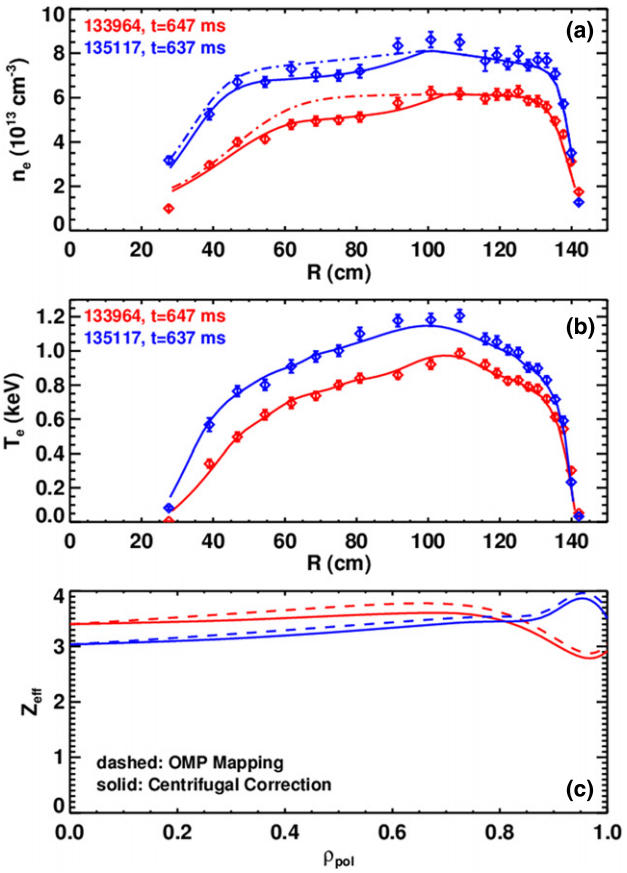

Figure 24. Study of centrifugal effects on the $Z_{\rm eff}$ profile for two high-performance discharges. Shown are the (*a*) electron density and (*b*) temperature profiles versus major radius across the midplane and the (*c*) mapped $Z_{\rm eff}$ profiles.

rotation frequency was taken to be equal to that for carbon; this could be resolved by taking the neoclassical deuterium toroidal rotation velocity from TRANSP, at the expense of increasing the complexity of the calculation. Once the deuterium, carbon and electron densities are known as a function of poloidal angle on each magnetic surface, $Z_{\rm eff}(\theta)$ can be computed. The flux-surface average can then be calculated, providing the radial profile of $\langle Z_{\rm eff}\rangle$ for calculations of the current components.

An example of these calculations is shown in figure 24, for time slices from the high-$\beta_{\rm P}$ shot 133964 (figure 12) and high-$\beta_{\rm T}$ shot 135117 (figure 19(*b*)). Frame (*a*) shows the measured density profiles across the midplane. The dashed line shows a fit where only the data on the OMP were used as a constraint. The fit matches well on the outboard side, but clearly overestimates the data on the inboard side. The solid lines show the midplane electron density from the iterative solution of equation [4], where a significantly improved fit to both sides of the profile is achieved. For reference, the electron temperature profiles are shown in frame (*b*), where the fit is derived from both the inboard and outboard sides; no significant inboard/outboard error is seen, as expected given the high parallel thermal conductivity.

The $Z_{\rm eff}$ profiles for these two cases are shown in frame (*c*), where the dashed line uses simple outboard midplane mappings, and the solid line uses the flux-surface average of the poloidally mapped species densities. The calculation with centrifugal corrections shows a slight reduction in $Z_{\rm eff}$. Inclusion of the effect in calculations of the total inductive current typically yields a $\sim$10 kA increase, which is $\sim$1% of the total current. This explains a small amount of the discrepancy in the total current accounting noted in multiple places above. Given the marginal benefit and additional complexity of this centrifugal correction, we have not applied it to the calculations presented in sections 3–6. The calculation does show, however, that centrifugal effects continue to be important in determining the profile shapes in these high-performance plasmas.

In summary, the results presented in this paper demonstrate that, in the absence of low-frequency MHD activity, the current profile in NSTX high-β plasmas can be understood using (neo)classical physics only. This result holds over a range of q_{95}. However, when low-frequency MHD is present, the addition of some anomalous diffusion of the beam ions is required. The results do not, however, exclude the possibility of some small level of fast-ion diffusivity ($D_{\rm FI} <\sim$ 0.5–2 m^2 s^{-1}) in discharge free of low-frequency MHD. Diffusivities at this level or smaller could have a significant effect on the current drive localization for off-axis neutral beams. The proposed NSTX-Upgrade [125] could provide important additional information on this topic by providing six total NB sources with tangency radii from 50 to 130 cm, enabling off-axis NBCD studies in full-sized, high-β ST plasmas.

Acknowledgments

The authors wish to acknowledge Dennis Mueller, Roger Raman and Tim Stevenson for their skilled operation of NSTX during these experiments, and thank Bill Heidbrink for his useful comments. This research was funded by United States Department of Energy Contract D-AC02-09CH11466.

Appendix A. Modelling of the USXR emission from coupled kink-tearing modes

The modelling of the USXR emission due to the coupled 2/1 + 1/1 modes requires two steps: (i) calculation of the USXR emission, to calculate the emissivity as a function of minor radius (normalized poloidal flux), (ii) construction of a model eigenfunction for the MHD mode and (iii) mapping of the emissivity to the eigenfunction and integrating along the USXR detector lines of sight.

The USXR emission is calculated via an inversion of the chordal emission, averaged over many instances of the mode structure rotating in front of the detector array. A regularized inversion scheme is used, in order to find an emission profile that is radially smooth but consistent with the chordal emission. No attempt is made to compute the emission from a first principle emission calculation. The net result of this step is the emission as a function of normalized poloidal flux.

The mode eigenfunction in this calculation is composed of both a core $m/n = 1/1$ kink and a 2/1 magnetic island. The 2/1 island is modelled via the method described in [103]: the helical flux is computed, a perturbation resonant with the 2/1 surface is imposed, and the island structure is computed. The radius of the island chain is determined by the location of the $q = 2$ surface, and the width of the islands is set by adjusting

the amplitude of the helical flux to match the observed USXR emission contours.

The $m/n = 1/1$ perturbation is then added to the model. The displacement is modelled as a rigid perturbation to the helical flux function in the plasma core, whose radial structure is given by

$$\xi_{1,1} = \begin{cases} \xi_0, & r < r_c, \\ \xi_0 e^{-[(r-r_c)/r_f]^2}, & r > r_c. \end{cases}$$

The parameters r_c, r_f and ξ_0 determine the radial region of the perturbation, the radial fall-off width and the size of the shift. The phase of the 1/1 perturbation is generally set so that the displacement is in the large major-radius direction at toroidal angles where one of the 2/1 mode X-points is on the outboard side. We note that this is not a theory based model for the 1/1 mode; the merit of this approach is that it allows easy comparison with the measurements.

The emission function previously calculated is then mapped onto the new equilibrium with the island/kink; the emission is assumed to be constant within the island. The emission is then integrated along the line of sight of the USXR detectors, for different phases of the coupled 2/1+1/1 structure with respect to the toroidal angle of the USXR array, in order to simulate the effect of plasma rotation. For instance, the calculation in figure 9 used 24 toroidal phases between 0 and 2π to provide good resolution along the x-axis. A fast Fourier transform of the USXR signals is then taken, in order to precisely find the frequency of the dominant perturbation. This frequency is used to assign a series of times to the calculations of the different mode-detector phase, allowing the direct comparison of the simulation with data in figure 9.

References

[1] Peng Y.K.M. and Strickler D.J. 1986 *Nucl. Fusion* **26** 769
[2] Goldston R.J. *et al* 2008 An experiment to tame the plasma material interface *Proc. 22nd Int. Conf. on Fusion Energy 2008 (Geneva, Switzerland, 2008)* (Vienna: IAEA) CD-ROM file FT/P3-12 and http://www-naweb.iaea.org/napc/physics/FEC/FEC2008/html/index.htm
[3] Abdou M. 1995 *Fusion Eng. Des.* **27** 111
[4] Wilson H.R. *et al* 2004 A steady state spherical tokamak for components testing *Proc. 20th Int. Conf. on Fusion Energy 2004 (Vilamoura, Portugal, 2004)* (Vienna: IAEA) CD-ROM file FT/3-1Ra and http://www-naweb.iaea.org/napc/physics/fec/fec2004/datasets/index.html
[5] Peng Y-K.M. *et al* 2005 *Plasma Phys. Control. Fusion* **47** B263
[6] Voss G.M. *et al* 2008 *Fusion Eng. Des.* **83** 1648
[7] Peng Y.K.M. *et al* 2008 Extensive remote handling and conservative plasma conditions to enable fusion nuclear science R&D using a component testing facility *Proc. 22nd Int. Conf. on Fusion Energy 2008 (Geneva, Switzerland, 2008)* (Vienna: IAEA) CD-ROM file FT/P3-14 and http://www-naweb.iaea.org/napc/physics/FEC/FEC2008/html/index.htm
[8] Najmabadi F. and the ARIES Team 2003 *Fusion Eng. Des.* **65** 143
[9] Jardin S.C. *et al* 2003 *Fusion Eng. Des.* **65** 165
[10] Sykes A. *et al* 1992 *Nucl. Fusion* **32** 694
[11] Gryaznevich M. *et al* 1998 *Phys. Rev. Lett.* **80** 3972
[12] Gates D.A. *et al* 1998 *Phys. Plasmas* **5** 1775
[13] Akers R.J. *et al* 2002 *Nucl. Fusion* **42** 122
[14] Miller R.L. *et al* 1997 *Phys. Plasmas* **4** 1062
[15] Menard J.E. *et al* 1997 *Nucl. Fusion* **37** 595
[16] Bickerton R.J., Connor J.W. and Taylor J.B. 1971 *Nature Phys. Sci.* **229** 110
[17] Galeev A.A. 1971 *Sov. Phys.—JETP* **32** 752
[18] Zarnstorff M.C. and Prager S.C. 1984 *Phys. Rev. Lett.* **53** 454
[19] Kessel C.E. 1994 *Nucl. Fusion* **34** 1221
[20] Peeters A.G. 2000 *Plasma Phys. Control. Fusion* **42** B231
[21] Ono M. *et al* 2000 *Nucl. Fusion* **40** 557
[22] Sykes A. *et al* 2001 *Nucl. Fusion* **41** 11
[23] Forrest C.B. *et al* 1994 *Phys. Rev. Lett.* **73** 2444
[24] Sauter O., Angioni C. and Lin-Liu Y.R. 1999 *Phys. Plasmas* **6** 2834
[25] Hirshman S.P. 1988 *Phys. Fluids* **31** 3150
[26] Houlberg W.A. *et al* 1997 *Phys. Plasmas* **4** 3230
[27] Ohkawa T. 1970 *Nucl. Fusion* **10** 185
[28] Start D.F. *et al* 1978 *Phys. Rev. Lett.* **40** 1497
[29] Start D.F.H. and Cordey J.G. 1980 *Phys. Fluids* **23** 1477
[30] Start D.F.H., Cordey J.G. and Jones E.M. 1980 *Plasma Phys.* **22** 303
[31] Fisch N.J. 1987 *Rev. Mod. Phys.* **59** 175
[32] Heidbrink W.W. and Sadler G.J. 1994 *Nucl. Fusion* **34** 535
[33] Lin-Liu Y.R. and Hinton F.L. 1997 *Phys. Plasmas* **4** 4179
[34] Goldston R.J. *et al* 1981 *J. Comput. Phys.* **43** 61
[35] Pankin A. *et al* 2004 *Comput. Phys. Commun.* **159** 157
[36] Politzer P.A. 1994 *Phys. Plasmas* **1** 1545
[37] Forest C.B. *et al* 1997 *Phys. Rev. Lett.* **79** 427
[38] Luce T.C. 1999 *Plasma. Phys. Control. Fusion* **41** B119
[39] Petty C.C. *et al* 1999 *Nucl. Fusion* **39** 1421
[40] Petty C.C. 2000 *Plasma Phys. Control. Fusion* **42** B75
[41] Wade M.R. *et al* 2001 *Phys. Plasmas* **8** 2208
[42] Carolipio E.M. *et al* 2002 *Nucl. Fusion* **42** 853
[43] Greenfield C.M. *et al* 2004 *Phys. Plasmas* **11** 2616
[44] Murakami M. *et al* 2005 *Nucl. Fusion* **45** 1419
[45] Luce T.C. for the DIII-D Team 2005 *Nucl. Fusion* **45** S86
[46] Doyle E.J. *et al* 2006 *Plasma Phys. Control. Fusion* **48** B39
[47] Murakami M. *et al* 2009 *Nucl. Fusion* **49** 065031
[48] Park J.M. *et al* 2009 *Phys. Plasmas* **16** 092508
[49] Heidbrink W.W. *et al* 2009 *Phys. Rev. Lett.* **103** 175001
[50] Heidbrink W.W. *et al* 2009 *Plasma Phys. Control. Fusion* **51** 125001
[51] Holcomb C.T. *et al* 2009 *Phys. Plasmas* **16** 056116
[52] Challis C.D. *et al* 1989 *Nucl. Fusion* **29** 563
[53] Joffrin E. *et al* 2005 *Nucl. Fusion* **45** 626
[54] Litaudon X. *et al* 2007 *Nucl. Fusion* **47** 1285
[55] Chapman I.T. *et al* 2008 *Plasma Phys. Control. Fusion* **50** 045006
[56] Voitsekhovitch I. *et al* 2009 *Nucl. Fusion* **49** 055026
[57] Oikawa T. *et al* 2000 *Nucl. Fusion* **40** 435
[58] Suzuki T. *et al* 2008 *Nucl. Fusion* **48** 045002
[59] Zarnstorff M.C. *et al* 1990 *Phys. Fluids* B **2** 1852
[60] Günter S. *et al* 2007 *Nucl. Fusion* **47** 920
[61] Garcia-Munoz M. *et al* 2009 *Nucl. Fusion* **49** 085014
[62] Garcia-Munoz M. *et al* 2009 *Nucl. Fusion* **47** L10
[63] Wong K.L. *et al* 2004 *Phys. Rev. Lett* **93** 085002
[64] Wong K.L. *et al* 2005 *Nucl. Fusion* **45** 30
[65] Turnyanskiy M. *et al* 2009 *Nucl. Fusion* **49** 065002
[66] Hawryluk R.J. *et al* 1980 An empirical approach to tokamak transport *Physics of Plasmas Close to Thermonuclear Conditions* vol 1, ed B. Coppi *et al* (Brussels: CEC) pp 19–46
[67] Menard J.E. *et al* 2006 *Phys. Rev. Lett* **97** 095002
[68] Menard J.E. *et al* 2007 *Nucl. Fusion* **47** S645
[69] Gates D.A. *et al* 2007 *Nucl. Fusion* **47** 1376
[70] Kaye S.M. *et al* 2005 *Nucl. Fusion* **45** S168
[71] Bell M.G. *et al* 2006 *Nucl. Fusion* **46** S565
[72] Gates D.A. *et al* 2006 *Phys. Plasmas* **13** 056122
[73] Gates D.A. *et al* 2009 *Nucl. Fusion* **49** 104016
[74] Heidbrink W.W. *et al* 2003 *Nucl. Fusion* **43** 883
[75] Gates D.A. *et al* 2003 *Phys. Plasmas* **10** 1659
[76] Gates D.A. *et al* 2006 *Nucl. Fusion* **46** S22
[77] Gates D.A. *et al* 2006 *Nucl. Fusion* **46** 17
[78] Menard J.E. *et al* 2010 *Nucl. Fusion* **50** 045008

[79] Gerhardt S.P. *et al* 2010 *Plasma Phys. Control. Fusion* **52** 104003
[80] Sabbagh S.A. *et al* 2006 *Phys. Rev. Lett.* **97** 045004
[81] Sabbagh S.A. *et al* 2010 *Nucl. Fusion* **50** 025020
[82] Gerhardt S.P. *et al* 2010 Performance of discharges with high elongation and beta in NSTX and near-term paths toward steady state *IAEA Fusion Energy Conf. (Seoul, Korea)* Paper EXS/P2-08
[83] Kugel H.W. *et al* 2008 *Phys. Plasmas* **15** 056118
[84] Bell M. *et al* 2009 *Plasma Phys. Control. Fusion* **51** 124054
[85] Maingi R. *et al* 2009 *Phys. Rev. Lett.* **103** 075001
[86] Ding S. *et al* 2010 *Plasma Phys. Control. Fusion* **52** 015001
[87] Maingi R. *et al* 2010 *Nucl. Fusion* **50** 064010
[88] LeBlanc B.P. *et al* 2003 *Rev. Sci. Instrum.* **74** 1659
[89] Levinton F. and Yuh H. 2008 *Rev. Sci. Instrum.* **79** 10F522
[90] http://w3.pppl.gov/~jmenard/software/lrdfit/lrdfit-index.htm
[91] Sauter O., Angioni C. and Lin-Liu Y.R. 2002 *Phys. Plasmas* **9** 5140
[92] Heidbrink W.W. *et al* 1991 *Phys. Fluids* B **3** 3167
[93] Suzuki T. *et al* 2010 Experimental investigation and validation of neutral beam current drive for ITER through ITPA joint experiments *IAEA Fusion Energy Conf. (Seoul, Korea)* Paper ITR/P1-14
[94] Podesta M. *et al* 2009 *Phys. Plasmas* **16** 056104
[95] Bortolon A. *et al* 2010 *Rev. Sci. Instrum.* **81** 10D728
[96] Fredrickson E.D. *et al* 2009 *Phys. Plasmas* **16** 122505
[97] Fredrickson E.D. *et al* 2006 *Phys. Plasmas* **13** 056109
[98] Cheng C.Z. 1992 *Phys. Rep.* **211** 1
[99] Gorelenkov N.N., Cheng C.Z. and Fu G.Y. 1999 *Phys. Plasmas* **2** 2802
[100] White R.B. and Chance M.S. 1984 *Phys. Fluids* **27** 2455
[101] Smith D.R. *et al* 2010 *Rev. Sci. Instrum.* **81** 10D717
[102] Stutman D. *et al* 1999 *Rev. Sci. Instrum.* **70** 572
[103] Menard J.E. *et al* 2005 *Nucl. Fusion* **45** 539
[104] Gerhardt S.P. *et al* 2009 *Nucl. Fusion* **49** 025005
[105] Buttery R.J. *et al* 2008 *Phys. Plasmas* **15** 056115
[106] La Haye R.J. and Buttery R.J. 2009 *Phys. Plasmas* **16** 022107
[107] La Haye R.J. *et al* 2010 *Phys. Plasmas* **17** 056110
[108] Chapman I.T. *et al* 2010 *Nucl. Fusion* **50** 045007
[109] Fredrickson E.D. 2002 *Phys. Plasmas* **9** 548
[110] Meskat J.P. *et al* 2001 *Plasma Phys. Control. Fusion* **43** 1325
[111] Brennan D. *et al* 2007 *Phys. Plasmas* **14** 056108
[112] Mynick H.E. 1993 *Phys. Fluids* B **5** 1476
[113] Zweben S.J. *et al* 1999 *Nucl. Fusion* **39** 1097
[114] Gobbin M. *et al* 2009 *Nucl. Fusion* **49** 095021
[115] Zhang W. *et al* 2008 *Phys. Rev. Lett.* **101** 095001
[116] Hauff T. *et al* 2009 *Phys. Rev. Lett.* **102** 075004
[117] Gorelenkov N.N. *et al* 2004 *Phys. Plasmas* **11** 2586
[118] Fredrickson E.D. *et al* 2004 *Phys. Plasmas* **11** 3563
[119] Fredrickson E.D. *et al* 2006 *Nucl. Fusion* **46** S926
[120] Stutman D. *et al* 2009 *Phys. Rev. Lett.* **102** 115002
[121] Gates D.A. *et al* 2001 *Phys. Rev. Lett.* **88** 205003
[122] Waltz R.E. *et al Phys. Plasmas* **4** 2482 (3230)
[123] Staebler G.M., Colyer G., Kaye S., Kinsey J.E. and Waltz R.E. 2008 Testing the trapped gyro-Landau fluid transport model with data from tokamaks and spherical tori *Proc. 22nd Int. Conf. on Fusion Energy 2008 (Geneva, Switzerland, 2008)* (Vienna: IAEA) CD-ROM file TH/P8-42 and http://www-naweb.iaea.org/napc/physics/FEC/FEC2008/html/index.htm
[124] Wesson J.A. 1997 *Nucl. Fusion* **37** 577
[125] Menard J.E. *et al* Physics design of NSTX Upgrade *37th European Physical Society Conf. on Plasma Physics (Dublin, Ireland)* and http://ocs.ciemat.es/EPS2010PAP/pdf/P2.106.pdf